nature neuroscience

Technical Report

https://doi.org/10.1038/s41593-026-02325-w

Red-shifted GRAB acetylcholine sensors for multiplex imaging in vivo

Received: 4 December 2024

Accepted: 6 May 2026

Published online: 16 June 2026

Check for updates

Shu Xie (谢书)[1,2,3,7], Xiaolei Miao (苗晓蕾)[1,2,4,7], Guochuan Li (李国川)[1,5,7], Yu Zheng (郑宇)[1,2,3], Mengyao Li (李梦尧)[1,2], En Ji (纪恩)[1,2,3], Jinxu Wang (王金旭)[1,2,4], Shaochuang Li (李少创)[1,2,3], Ruyi Cai (蔡儒仪)[1,2,3], Lan Geng (耿岚)[1,2,3], Jiesi Feng (冯杰思)[1,2,3], Changwei Wei (魏昌伟)[4] ✉ & Yulong Li (李毓龙)[1,2,3,5,6] ✉

The neurotransmitter acetylcholine (ACh) is essential in both the central and peripheral nervous systems. Recent studies highlight the significance of interactions between ACh and various neuromodulators in regulating complex behaviors. The ability to simultaneously image ACh and other neuromodulators can provide valuable information regarding the mechanisms underlying these behaviors. Here we developed a series of red fluorescent G-protein-coupled receptor activation-based ACh sensors, with a wide detection range and expanded spectral profile. The high-affinity sensor rACh1h reliably detects ACh release in various brain regions, including the nucleus accumbens, amygdala, hippocampus and cortex. Moreover, rACh1h can be coexpressed with green fluorescent sensors to record ACh release together with other neurochemicals in various behavioral contexts using fiber photometry, mesoscopic imaging and two-photon imaging with high spatiotemporal resolution.

Acetylcholine (ACh), the first neurotransmitter to be identified, plays important roles in both the central and peripheral nervous systems[1–6]. In the brain, cholinergic neurons are involved in diverse functions, including attention, locomotion, associative learning and regulating the sleep–wake cycle[6–8]. In addition, the interaction between ACh and other neurochemicals has been reported to mediate motivation, cue detection and reinforcement learning[9,10]. In the striatum, the release of ACh can be inhibited by dopamine (DA) through DA D2 receptors[11,12], whereas it is driven by glutamate (Glu) inputs from the cortex and thalamus[13]. This modulation of DA and Glu on ACh is essential for decision-making and learning processes[11]. Pioneer research also indicated that the interaction between ACh and oxytocin in the hippocampus is crucial for regulating brain states[14]. The simultaneous imaging of ACh and other neurochemicals has provided valuable insights into the regulation of brain functions controlled by these signaling processes[15]. Such investigations are helpful in identifying new drug targets and developing innovative therapeutic strategies for neural diseases[16]. Current state-of-the-art green ACh sensors such as G-protein-coupled receptor activation-based $(GRAB)_{ACh3.0}$ and iAChSnFR are based on green fluorescent proteins and have been used to measure ACh in vivo[17–19]; however, a red fluorescent ACh sensor would be extremely valuable due to its spectral compatibility with green fluorescent sensors, allowing for the simultaneous detection of ACh and other neurochemicals.

Here we developed a series of red fluorescent ACh sensors. These red-shifted sensors, which we call rACh1h, rACh1m and rACh1l (with high, medium and low ACh affinity, respectively), have a 5-fold increase in fluorescence in response to ACh. We then compared the performance—including the response to ACh and the signal-to-noise ratio (SNR)—of these red fluorescent ACh sensors with $GRAB_{ACh3.0}$ and iAChSnFR. We also showed that rACh1h can be used to monitor both

[1]State Key Laboratory of Membrane Biology, School of Life Sciences, Peking University, Beijing, China. [2]PKU-IDG/McGovern Institute for Brain Research, Beijing, China. [3]Peking-Tsinghua Center for Life Sciences, New Cornerstone Science Laboratory, Academy for Advanced Interdisciplinary Studies, Peking University, Beijing, China. [4]Department of Anesthesiology, Beijing Chaoyang Hospital, Capital Medical University, Beijing, China. [5]Peking University Chengdu Academy for Advanced Interdisciplinary Biotechnologies, Chengdu, China. [6]National Biomedical Imaging Center, Peking University, Beijing, China. [7]These authors contributed equally: Shu Xie, Xiaolei Miao, Guochuan Li. ✉e-mail: changwei.wei@ccmu.edu.cn; yulongli@pku.edu.cn

spontaneous and optogenetically evoked endogenous ACh release in vivo using fiber photometry. When coupled with green GRAB sensors in dual-color recordings, rACh1h revealed a strong correlation between ACh and DA signals in Pavlovian conditioning tasks, as well as distinct dynamics of ACh and serotonin (5-HT) in sleep–wake cycles. Furthermore, multiplex imaging using mesoscopic microscopy and two-photon microscopy elucidated the release patterns of ACh and norepinephrine (NE) across various behaviors in the dorsal cortex. Thus, these red-shifted sensors provide a new toolkit for investigating the functional roles of ACh in neural system.

Results

Development and characterization of red ACh sensors

To expand the spectral profile of $GRAB_{ACh}$ sensors, we generated a series of red fluorescent ACh sensors. We began by transplanting the cpmApple module from the red fluorescent DA sensor $rGRAB_{DA}$ into the third intracellular loop of the mouse type 3 muscarinic ACh receptor (M_3R) (Fig. 1a), followed by systematic optimization of both the receptor and the fluorescent module[20–22] (Supplementary Fig. 1). Screening approximately 2,000 variants using the ACh-induced change in fluorescence led to the low-affinity rACh1l ACh sensor. Given that the green fluorescent GRAB sensor ACh3.0, which is based on human M_3R, produces a large change in fluorescence upon binding ACh[18], we attempted to improve the response and affinity of the red fluorescent sensor using a chimeric strategy in which we fused the sequence of human M_3R before the $V198^{4.55}$ site with rACh1l after the $V197^{4.55}$ site[21] (superscript indicates Ballesteros–Weinstein numbering system[23]). Screening >1,000 candidates using the ACh-induced change in fluorescence and the affinity index (see Methods for details), we obtained a high-affinity rACh1h sensor, which has an improved response and higher affinity compared to rACh1l. We then generated a medium-affinity sensor, rACh1m, by introducing the $N513^{6.58}$ K substitution in rACh1h. Finally, we introduced the $W199^{4.57}$ T mutation in rACh1h to create an ACh-insensitive version, rAChmut, to serve as a negative control.

We then expressed these rACh sensors in HEK293T cells and characterized their spectral properties using both one-photon and two-photon excitation. We found that rACh1h has excitation peaks at 565 nm (one photon) and 1,050 nm (two photons) (Fig. 1b). Similarly, rACh1m and rACh1l exhibit one-photon excitation peaks at 560 nm, with two-photon excitation peaks at 1,060 nm and 1,110 nm, respectively (Supplementary Fig. 2a,b). The red fluorescent ACh sensors have a robust increase in fluorescence ($\Delta F/F_0$) in response to 100-μM ACh, with rACh1h having a 5-fold $\Delta F/F_0$ relative to gACh3.0; in contrast, ACh has no effect when applied to cells expressing rAChmut (Fig. 1c,d and Supplementary Fig. 2c,d). Importantly, rACh1h has a greater response to ACh, with a higher SNR, than both gACh3.0 and iAChSnFR. Specifically, dose–response curves showed that rACh1h has a half-maximum effective concentration (EC_{50}) of ~0.4 μM compared to 2.2 μM and 8.8 μM for gACh3.0 and iAChSnFR, respectively (Fig. 1e). Moreover, rACh1m and rACh1l have EC_{50} values of ~1.2 μM and 4 μM, respectively (Supplementary Fig. 2e).

After being released from the presynaptic terminal, ACh is degraded to choline by acetylcholinesterase in the synaptic cleft[24]. We therefore measured the selectivity of ACh sensors for ACh over choline and found that our red fluorescent ACh sensors inherited the parent receptor's pharmacological specificity and had no detectable response to choline, whereas iAChSnFR responded to both ACh and choline (Fig. 1f and Supplementary Fig. 2f). Furthermore, the red fluorescent ACh sensors did not respond to any other signaling molecules tested, including a wide variety of neurotransmitters and neuromodulators (Fig. 1f and Supplementary Fig. 2g). Next, we assessed the photostability of rACh1h in cultured HEK293T cells. Under confocal laser illumination, rACh1h showed greater photostability than mApple, both with and without ACh (Extended Data Fig. 1a–c). Under wide-field light-emitting diode (LED) illumination, rACh1h was more photostable than mApple in saline but showed reduced photostability in the presence of ACh (Extended Data Fig. 1d–f). Upon ligand binding, rACh1h and RdLight1[25] exhibit reduced photostability compared with the ligand-free state under both confocal and wide-field imaging. Previous studies found that cpmApple-based sensors can be photoswitched by blue light[26,27]. To assess whether the rACh sensors exhibit photoswitching, we illuminated them with 488-nm light in the presence or absence of 100-μM ACh. We found that the rACh sensors showed largely attenuated response to blue light (with $\Delta F/F_0$ values of ~0.05, ~0.03 and ~0.005 for rACh1h, rACh1m and rACh1l, respectively), compared to an ~0.25 increase in jRGECO1a fluorescence (Fig. 1g and Extended Data Fig. 1g).

To measure the kinetics of our red fluorescent ACh sensors, we expressed them in HEK293T cells and performed rapid line-scanning microscopy while applying a local puff of ACh (to measure the activation-time constant, τ_{on}), followed by the ACh receptor antagonist

Fig. 1 | Development and performance of red $GRAB_{ACh}$ sensors. a, The predicted structure generated using AlphaFold[62] (left) and development of red ACh sensors (right). **b**, One-photon (left) and two-photon (right) excitation and emission spectra of rACh1h in the absence (dashed line) or presence (solid line) of 100-μM ACh. **c**, Representative images showing expression (top) and response to 100-μM ACh (bottom) of rACh1h, rAChmut, gACh3.0 and iAChSnFR. Scale bar: 20 μm. **d**, Quantification of relative $\Delta F/F_0$ and SNR of rACh1h, rAChmut, gACh3.0 and iAChSnFR before and after the addition of 100-μM ACh. Mean ± s.e.m. $n = 6, 5, 7$ and 6 coverslips for rACh1h, rAChmut, gACh3.0 and iAChSnFR, respectively. One-way analysis of variance (ANOVA) with post hoc Tukey's test was performed. Post hoc test: for $\Delta F/F_0$, $P = 4.83 \times 10^{-7}$, 6.90×10^{-7} and 2.95×10^{-7} for rACh1h versus rAChmut, gACh3.0 and iAChSnFR, respectively; for SNR, $P = 3.70 \times 10^{-5}$, 2.52×10^{-4} and 4.25×10^{-5} for rACh1h versus rAChmut, gACh3.0 and iAChSnFR, respectively. **e**, Normalized dose–response curves of rACh1h, rAChmut, gACh3.0 and iAChSnFR. Mean ± s.e.m. $n = 3$ wells for each sensor, with 300–500 cells per well. **f**, Pharmacological specificity of rACh1h in HEK293T cells. Antagonists were applied at 100 μM, others at 10 μM. $n = 3$ wells for rACh1h, 300–500 cells per well. Mean ± s.e.m. One-way ANOVA with post hoc Tukey's test was performed. Post hoc test: $P = 1 \times 10^{-208}$ for ACh versus ACh + Tio, ACh + Scop and other compounds. The insets show dose–response curves for ACh and choline. Mean ± s.e.m. $n = 3$ wells with 300–500 cells per well each. **g**, Representative traces (left) and peak $\Delta F/F_0$ (right) in response to blue light in cells expressing jRGECO1a, rACh1h, rACh1m and rACh1l. Mean ± s.e.m. $n = 5$ wells for each sensor. One-way ANOVA with post hoc Tukey's test was performed. Post hoc test: $P = 2.17 \times 10^{-4}$, 9.64×10^{-5} and 1.56×10^{-5} for jRGECO1a versus rACh1h, rACh1m and rACh1l. **h**, Kinetics measurements of rACh1h. Left: schematic illustration showing the experimental setup of line-scanning and local puffing. Scale bar: 20 μm. Middle: representative traces of sensor fluorescence increase in response to ACh (top) and decrease in response to Scop (bottom). Right: group summary of on and off kinetics for the sensors. Mean ± s.e.m. $n = 9$ puff tests for on kinetics; $n = 11$ puff tests for off kinetics. **i**, Downstream coupling test. Human M_3R; rACh1h; control, without expression of WT M_3R or sensors. For the luciferase complementation assay, mean ± s.e.m. $n = 3$ wells per group. One-way ANOVA with post hoc Tukey's test was performed. Post hoc test: $P = 1 \times 10^{-319}$ for rACh1h versus human M_3R. For the tango assay, mean ± s.e.m. $n = 3$ wells per group. One-way ANOVA with post hoc Tukey's test was performed. Post hoc test: $P = 1 \times 10^{-293}$ for rACh1h versus human M_3R. **j**, Left: representative images of cultured neurons expressing rACh1h. Scale bar: 20 μm. Right: expression and response of rACh1h, rAChmut, gACh3.0 and iAChSnFR in cultured neurons with the addition of 100-μM ACh. Scale bar: 20 μm. **k**, Group summary of $\Delta F/F_0$ and SNR of rACh1h, rAChmut, gACh3.0 and iAChSnFR. $n = 3$ wells for each sensor. Mean ± s.e.m. One-way ANOVA with post hoc Tukey's test was performed. For $\Delta F/F_0$, post hoc test: $P = 2.62 \times 10^{-7}$, 2.00×10^{-6} and 1.11×10^{-6} for rACh1h versus rAChmut, gACh3.0 and iAChSnFR, respectively. For SNR, post hoc test: $P = 0.011$, 0.019 and 0.015 for rACh1h versus rAChmut, gACh3.0 and iAChSnFR, respectively. **l**, Dose–response curves for ACh sensors. Mean ± s.e.m. $n = 3$ wells for each sensor. Ado, adenosine; complement., complementation; Em., emission; Ex., excitation; HA, histamine; OA, octopamine; NA, not available; NS, not significant; TA, tyramine; w/, with; w/o, without.

https://doi.org/10.1038/s41593-026-02325-w

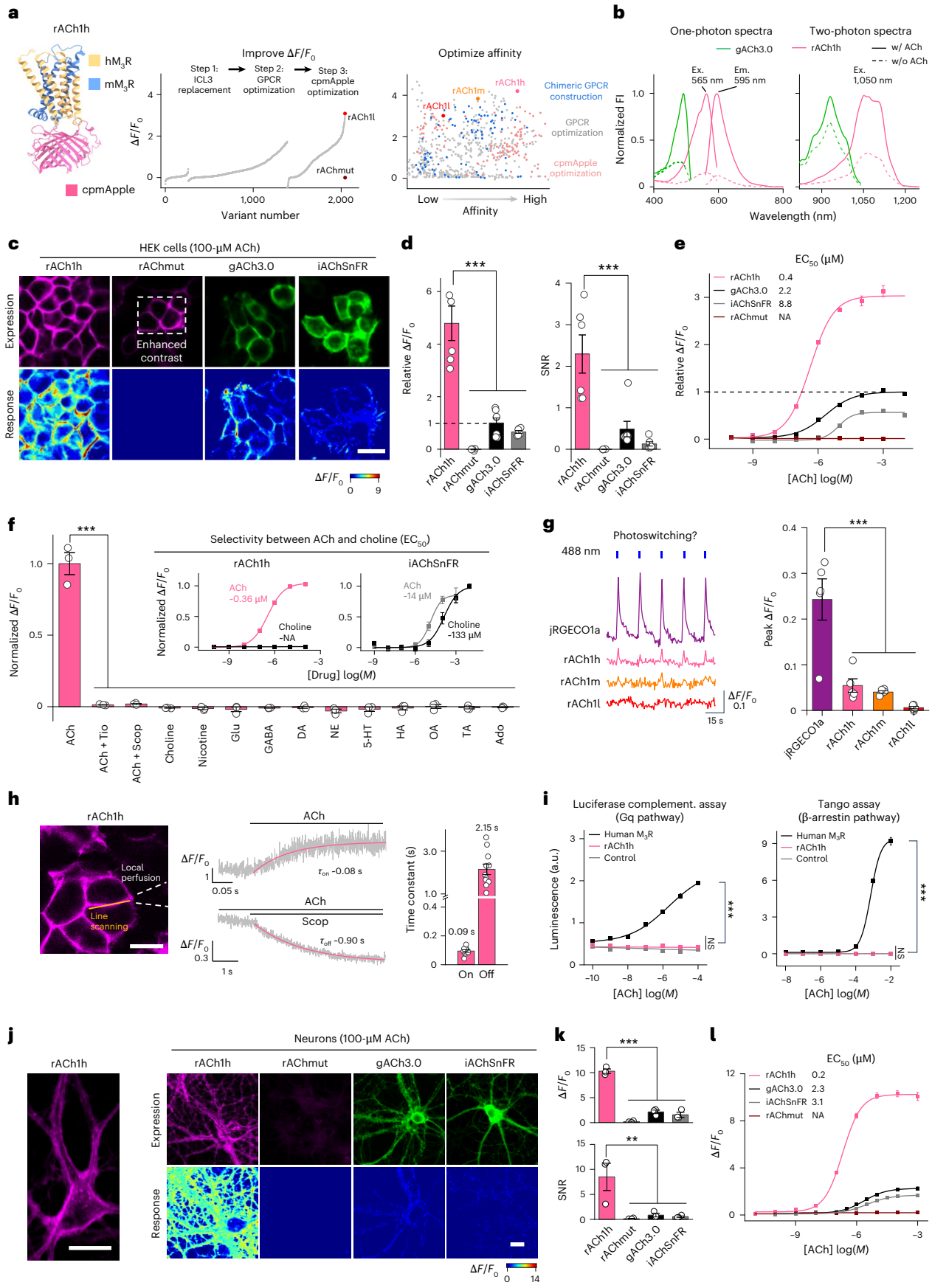

scopolamine (Scop; to measure τ_{off}) (Fig. 1h and Extended Data Fig. 2a–c). Our analysis revealed a τ_{on} value of approximately 0.1 s for all three ACh sensors and τ_{off} values ranging from 1.37 s to 2.15 s, reflecting the sensors' differences in affinity.

To confirm that the ACh sensors do not couple to downstream signaling pathways, we used the luciferase complementation assay[28] and the Tango assay[29] to measure the G protein and β-arrestin pathways, respectively. As expected, wild-type (WT) human M_3R exhibited robust coupling, whereas none of the three red fluorescent ACh sensors had measurable coupling (Fig. 1i and Extended Data Fig. 2d). Importantly, the ACh-induced increase in fluorescence was stable for at least 2 h, with minimal arrestin-mediated internalization (Extended Data Fig. 2e), indicating that these sensors can be used for long-term monitoring of ACh dynamics.

Next, we tested the performance of our ACh sensors in cultured cortical neurons. Consistent with our results obtained with HEK293T cells, all of the red fluorescent sensors were expressed at robust levels in the plasma membrane (Fig. 1j and Extended Data Fig. 2f). Moreover, upon application of 100-μM ACh, rACh1h, rACh1m and rACh1l exhibited a $\Delta F/F_0$ increase of 10.3, 8.0 and 6.8, respectively, whereas the ACh-insensitive rAChmut sensor had no detectable response (Fig. 1k and Extended Data Fig. 2g). In addition, rACh1h had a significantly higher fluorescence response and a higher SNR compared to both gACh3.0 and iAChSnFR. Dose–response curves measured in cultured neurons revealed EC_{50} values of ~0.2 μM, 0.5 μM and 2.8 μM for rACh1h, rACh1m and rACh1l, respectively (Fig. 1l and Extended Data Fig. 2h). Finally, and consistent with our findings in HEK293T cells, rACh1h had higher affinity compared to both gACh3.0 and iAChSnFR. Together, these data suggest that our red fluorescent ACh sensors are suitable for use in cultured neurons, and rACh1h outperforms existing green fluorescent ACh sensors in terms of response, SNR and ligand affinity.

Detecting ACh dynamics in acute brain slices

Prior studies showed that ACh plays an important functional role in the striatum[9,12,30]. To test whether our red-shifted ACh sensors can report the release of endogenous ACh, we injected an adeno-associated virus (AAV) expressing the rACh1h sensor into the nucleus accumbens (NAc), a structure that contains cholinergic interneurons. Three weeks after virus injection, we prepared acute brain slices and performed two-photon imaging while applying electrical stimuli to induce ACh release (Fig. 2a). We positioned the stimulating electrode in the NAc and applied increasing numbers of electrical pulses (delivered at 20 Hz) to the brain slice (Fig. 2b). We measured a stimulus-pulse-dependent increase in rACh1h fluorescence, with 100 pulses producing an increase of ~20%; moreover, the response was significantly inhibited by the muscarinic receptor antagonist tiotropium (Tio; 10 μM) (Fig. 2c,d). We then measured the kinetics of the change in rACh1h fluorescence in response to a single electrical pulse (Fig. 2e), with τ_{on} and τ_{off} values of ~0.08 s and 3.7 s, respectively (Fig. 2f). These results indicate that the rACh1h sensor can reliably detect the release of endogenous ACh in acute brain slices.

To determine whether the rACh1h sensor could sensitively report ACh release from individual sites, we expressed the rACh1h sensor specifically in cholinergic neurons using AAV-EF1α-DIO-rACh1h in the NAc (Extended Data Fig. 3a). The rACh1h sensor on cholinergic fibers exhibited a fluorescence increase upon electrical stimulation. This signal was enhanced by the K^+ channel blocker 4-AP and abolished by Cd^{2+}, confirming its dependence on Ca^{2+}-mediated ACh release (Extended Data Fig. 3b,c). Next, we combined minimal stimulation with imaging of rACh1h expressed in NAc acute brain slices[31–33] (Extended Data Fig. 3d,e). The fluorescence responses of rACh1h in artificial cerebrospinal fluid (ACSF) showed a bimodal distribution, with an additional peak shifted by approximately 6% $\Delta F/F_0$, which is indicative of discrete quantal events (Extended Data Fig. 3f–j). Control trials without stimulation and stimulation in the presence of Cd^{2+} exhibited a single peak in the distribution of responses at 0% $\Delta F/F_0$ (Extended Data Fig. 3k). The grouped data under minimal stimulation show this shifted peak (Extended Data Fig. 3l), supporting that rACh1h can resolve ACh release from individual sites.

Using red fluorescent ACh sensors to measure ACh release in vivo

Next, we examined whether our red fluorescent sensors can be used to monitor ACh release in vivo. Previous studies found that the basolateral amygdala (BLA) receives cholinergic input from the basal forebrain (BF)[4,34]. Therefore, to determine whether rACh1h can report ACh release in the BLA in vivo, we injected an AAV expressing either rACh1h or rAChmut (as a negative control) into the BLA and expressed the optogenetic tool channelrhodopsin-2 (ChR2)[35] in the BF (Fig. 2g). We then optically stimulated neurons in the BF and measured ACh signal in the BLA using fiber photometry. We found that rACh1h reliably detected both tonic ACh release and time-locked transient increases in ACh levels, with no detectable response in mice expressing rAChmut (Fig. 2h). Moreover, an intraperitoneal (i.p.) injection of the acetylcholinesterase inhibitor donepezil[36] (Done; 3 mg per kg) increased both the magnitude and duration of the rACh1h signal, whereas an i.p. injection of Scop (10 mg per kg) inhibited the rACh1h response (Fig. 2i–m). Notably, rACh1h's high affinity for ACh enabled it to detect spontaneous fluctuations in ACh (Fig. 2n). Fast Fourier transform analysis revealed that rACh1h can report spontaneous ACh release events occurring at a frequency

Fig. 2 | Detection of ACh dynamics ex vivo and in vivo. a, Schematic illustration depicting the two-photon imaging of acute brain slices prepared from mice expressing rACh1h in the NAc. An electrode placed in the NAc was used to evoke release of endogenous ACh. **b**, Representative images of expression and response to electrically evoked ACh. The dashed circles indicate the ROI used to calculate the response, and the approximate location of the stimulating electrode is indicated. Scale bars: left, 1 mm; right, 100 μm. **c**, Representative traces of the fluorescence change in rACh1h to electrical stimulation. Mean ± s.e.m. **d**, Group summary of the fluorescence change in rACh1h in response to electrical stimulation. Mean ± s.e.m. $n = 7$ slices from three mice. Two-tailed Student's *t*-tests: $P = 4.2 \times 10^{-5}$ for ACSF versus Tio at 100 pulses. **e**, Normalized representative trace of rACh1h in response to single-pulse electrical stimulation. **f**, Group summary of on and off kinetics of rACh1h. Mean ± s.e.m. $n = 6$ slices from three mice for on and off. **g**, Left: schematic illustration depicting the fiber-photometry recording involving red ACh sensors for **h**–**p**. Right: expression of rACh1h or rAChmut in the BLA and ChR2 in the BF. Scale bar: 1 mm. **h**, Representative traces of rACh1h and rAChmut in response to optical stimulation in the BF. Left: before (control). Middle: after an i.p. injection of the AChE inhibitor Done (3 mg per kg). Right: after an i.p. injection of the muscarinic receptor antagonist Scop (10 mg per kg). **i**, Representative trace of fluorescence change in rACh1h in response to Done application. **j**, Group summary of fluorescence change in rACh1h in response to Done application. Mean ± s.e.m. $n = 3$ mice for each rACh1h and rAChmut group. Two-tailed Student's *t*-tests: $P = 0.005$ of rACh1h before and after Done application. **k**, Representative trace of fluorescence change and kinetics in rACh1h in response to optogenetic stimulation. Mean ± s.e.m. **l**, Group summary of fluorescence change in rACh1h in response to optogenetic stimulation. Mean ± s.e.m. $n = 3$ mice for each rACh1h and rAChmut group. Two-tailed Student's *t*-tests were performed. $P = 0.04$ in rACh1h between control and Done, $P = 0.006$ in rACh1h between Done and Scop. **m**, Group summary of $decay_{t50}$ in rACh1h to optogenetic stimulation. Mean ± s.e.m. $n = 3$ mice. Two-tailed Student's *t*-tests were performed. $P = 6.6 \times 10^{-4}$ before and after Done application. **n**, Representative traces of rACh1h and rAChmut fluorescence before and after Scop application. **o**, Isolated power spectrum of rACh1h and rAChmut. Mean ± s.e.m. $n = 3$ mice for each rACh1h and rAChmut group. **p**, Area under the curve (AUC) for ACh power in the band at 0.02–1 Hz in rACh1h and rAChmut. Mean ± s.e.m. $n = 3$ mice for each rACh1h and rAChmut group. Two-tailed Student's *t*-tests were performed. $P = 0.02$ for rACh1h versus rAChmut. aco, anterior commissure, olfactory limb; P, pulse; Grab and i.p., grab the mouse and give an intraperitoneal injection. Illustrations in **a** and **g** created in BioRender; Li, Y. https://biorender.com/xngrhc6 (2026).

https://doi.org/10.1038/s41593-026-02325-w

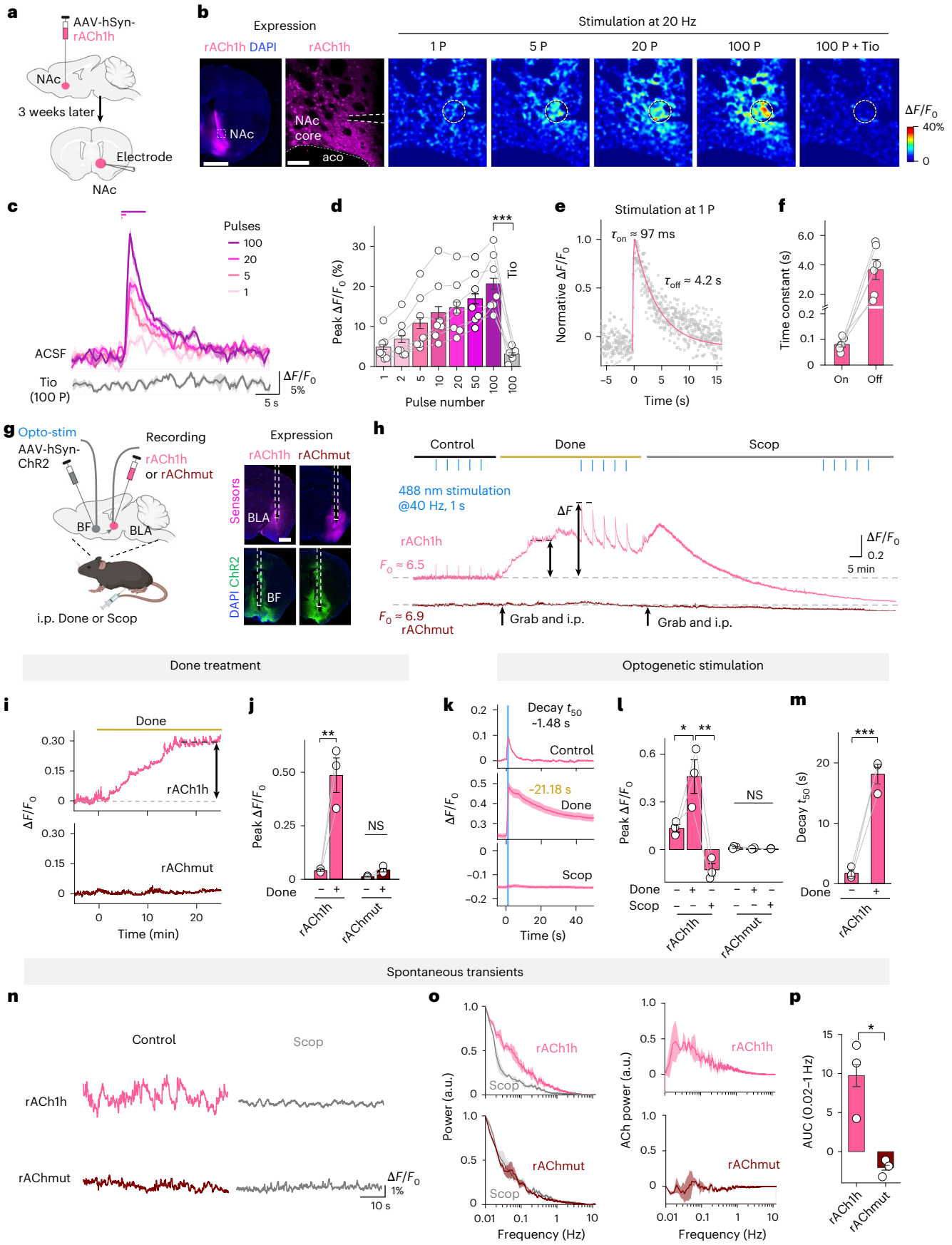

of 0.02–1 Hz, whereas no fluctuations were detected using rAChmut (Fig. 2o,p). We repeated these experiments using the medium-affinity and low-affinity rACh1m and rACh1l sensors (Extended Data Fig. 4a,b) and found that both sensors can reliably report the release of ACh from optically stimulated BF neurons (Extended Data Fig. 4c–h). Thus, all three red fluorescent ACh sensors can be used to monitor ACh release in vivo with high temporal resolution.

Dual-color recording of both ACh release and calcium signaling

We next determined whether the red fluorescent rACh1h sensor can be used together with the green fluorescent GCaMP6s sensor to simultaneously measure ACh release and changes in intracellular calcium, respectively. The modulation of medium spiny neurons by striatal cholinergic interneurons is critical for reinforcement learning and locomotion[37,38]. We therefore injected an AAV expressing rACh1h in the NAc while also expressing GCaMP6s in DA 1 receptor (D1R)–positive medium spiny neurons (Extended Data Fig. 5a). Using fiber photometry, we then recorded the rACh1h and GCaMP6s signals produced during both foot shock and reward paradigms. The results revealed that foot shock induced a robust increase in both rACh1h and GCaMP6s fluorescence, whereas reward induced a decrease in both rACh1h and GCaMP6s fluorescence, with a high correlation between the ACh and calcium signals (Extended Data Fig. 5b–e). The reward-associated decrease in ACh is consistent with previous reports[11–13]. To validate signal specificity, we showed that the muscarinic receptor antagonist tropicamide (Trop; 10 mg per kg) abolished this fluorescence decrease (Extended Data Fig. 5f,g). Furthermore, the rAChmut sensor exhibited no significant response to either foot shock or reward (Extended Data Fig. 5h,i), confirming that the rACh1h signals are driven by ACh dynamics.

Dual-color recording of both ACh and DA release

Leveraging the spectral compatibility of the red ACh sensor with green fluorescent sensors, we simultaneously monitored multiple signaling molecules within the same brain region. External reward and sensory cues trigger the release of both DA and ACh, both of which play an important role in facilitating learning and motivation[39]. Moreover, the BLA plays a key role in associating cues with both positive and negative valence outcomes[40]. To measure the release of these two neural modulators simultaneously in the BLA, we expressed rACh1h and gDA3h in the BLA and then used fiber photometry to record ACh and DA activity, respectively, during auditory Pavlovian conditioning tasks (Fig. 3a,b). We found that rACh1h responded to both reward and punishment, whereas gDA3h responded predominantly to reward. After 5 days of training, both sensors exhibited a stronger response to the tone predicting reward (Fig. 3c,d). Moreover, a cross-correlation analysis revealed a high correlation between the ACh and DA signals (Fig. 3e). In addition, both the rACh1h and gDA3h signals increased in response to the conditioned stimulus (CS) following training (Fig. 3f). This development of an increased response to reward-predicting cues is consistent with the so-called reward-prediction-error theory[41]. To validate the signal specificity in Pavlovian conditioning experiments, we coexpressed rAChmut and the gDA3h sensor in the BLA and performed the conditioning task (Extended Data Fig. 6a,b). In contrast to the robust responses seen with rACh1h, the rAChmut sensor showed no significant fluorescence changes in response to either the CS or the unconditioned stimulus (US) (Extended Data Fig. 6c–f). Together, these results confirmed that the red fluorescent rACh1h sensor is compatible for use with gDA3h, providing the ability to simultaneously measure ACh and DA release in real time.

Simultaneously measuring ACh and 5-HT release during the sleep–wake cycle

The hippocampus plays an essential role in memory consolidation during sleep and receives both cholinergic and serotonergic inputs[5,42]. To measure both ACh and 5-HT levels during the sleep–wake cycle, we injected AAVs expressing red fluorescent rACh1h and the green fluorescent 5-HT sensor g5-HT3.0 in the dorsal CA1 region (dCA1) of the hippocampus. We then performed simultaneous fiber photometry, electroencephalography (EEG; to measure the sleep–wake cycle) and electromyography (EMG; to measure the animal's activity) recordings in freely moving mice (Fig. 3g,h). We found that both the rACh1h and g5-HT3.0 signals were high during wakefulness but were relatively low during non-rapid eye movement (NREM) sleep. Moreover, during REM sleep, the rACh1h signal was high and the g5-HT3.0 signal was low (Fig. 3i), consistent with previous studies[18,22,43]. As a negative control, the ACh-insensitive rAChmut signal did not increase during REM sleep (Extended Data Fig. 7). An analysis of the transition between various sleep–wake states revealed a strong positive correlation between the rACh1h and g5-HT3.0 signals during the wake-to-NREM and NREM-to-wake transitions and a negative correlation during the NREM-to-REM transition (Fig. 3j,k). We also calculated the rise t_{50} (the time for a signal to reach 50% of its maximum value) and decay t_{50} (the time for a signal to decrease by 50% from its maximum value) of the signals during transitions between sleep–wake states and found that the ACh signal decreased more rapidly compared to the 5-HT signal during the wake-to-NREM transition (Fig. 3l).

Multiplex imaging ACh and NE dynamics in the dorsal cortex

Cholinergic and noradrenergic systems are crucial for cortical function. Cholinergic neurons in the BF innervate the neocortex, modulating

Fig. 3 | Multiplex measurements of ACh with other neuromodulators. **a**, Schematic illustration and expression image depicting the dual-color recording involving rACh1h and gDA3h during Pavlovian conditioning tasks shown in **b**–**f**. Scale bar: 1 mm. **b**, Representative traces of rACh1h (pink) and gDA3h (green) simultaneously measured in BLA during seven consecutive trials. **c**, Representative heatmaps and averaged traces of rACh1h and gDA3h fluorescence from a mouse in naive (top) and trained (bottom) states. The gray shading indicates the application of audio. The dashed line indicates the delivery of water, puff or nothing. **d**, Group-averaged traces of rACh1h and gDA3h in the BLA for all mice under naive and trained states. Mean ± s.e.m. $n = 4$ mice. **e**, The average cross-correlation between rACh1h and gDA3h signals under naive and trained states. Puff trials (blue), water trials (orange) and shuffled trace (black). Mean ± s.e.m. $n = 4$ mice. **f**, Group summary of fluorescence change of rACh1h and gDA3h signals to CS (left) and US (right). Mean ± s.e.m. $n = 4$ mice. Paired two-tailed Student's *t*-tests were performed. In the US, for rACh1h, $P = 0.045$ in nothing trial. In the CS, for rACh1h, $P = 0.012$ in water trial. For gDA3h, $P = 0.003$ in water trial, $P = 0.039$ in puff trial. **g**, Schematic illustration and expression image depicting the dual-color recording involving rACh1h and g5-HT3.0 during sleep–wake cycles for **h**–**l**. Scale bar: 1 mm. **h**, Representative traces of EEG, EMG, rACh1h (pink) and g5-HT3.0 (green) during sleep–wake cycles in freely behaving mice. Blue shading, wake state; orange shading, REM sleep. **i**, Group summary of rACh1h and g5-HT3.0 fluorescence in dCA1 during the wake state, NREM sleep and REM sleep. Mean ± s.e.m. $n = 4$ mice. One-way ANOVA with post hoc Tukey's test was performed. For rACh1h, post hoc test: $P = 7.5 \times 10^{-4}$ between wake and NREM, $P = 6.4 \times 10^{-4}$ between NREM and REM. For g5-HT3.0, post hoc test: $P = 2.2 \times 10^{-3}$ between wake and NREM, $P = 5.8 \times 10^{-5}$ between wake and REM, $P = 0.03$ between NREM and REM. **j**, Representative time courses of rACh1h and g5-HT3.0 fluorescence signal during the indicated transitions between the sleep–wake states. Mean ± s.e.m. **k**, Left: the average cross-correlation between rACh1h and g5-HT3.0 signals during sleep–wake cycles. Right: group summary of time lag of cross-correlation peak between rACh1h and g5-HT3.0 signals during sleep–wake cycles. Mean ± s.e.m. $n = 4$ mice. **l**, Group summary (left) and summary model (right) of the t_{50} values measured for each transition between the indicated sleep–wake states. Mean ± s.e.m. Two-tailed Student's *t*-tests were performed. $P = 2.7 \times 10^{-7}$ between rACh1h and g5-HT3.0 during the transition from wake to NREM. ITI, intertrial interval. Illustrations in **a** and **g** created in BioRender; Li, Y. https://biorender.com/xngrhc6 (2026).

https://doi.org/10.1038/s41593-026-02325-w

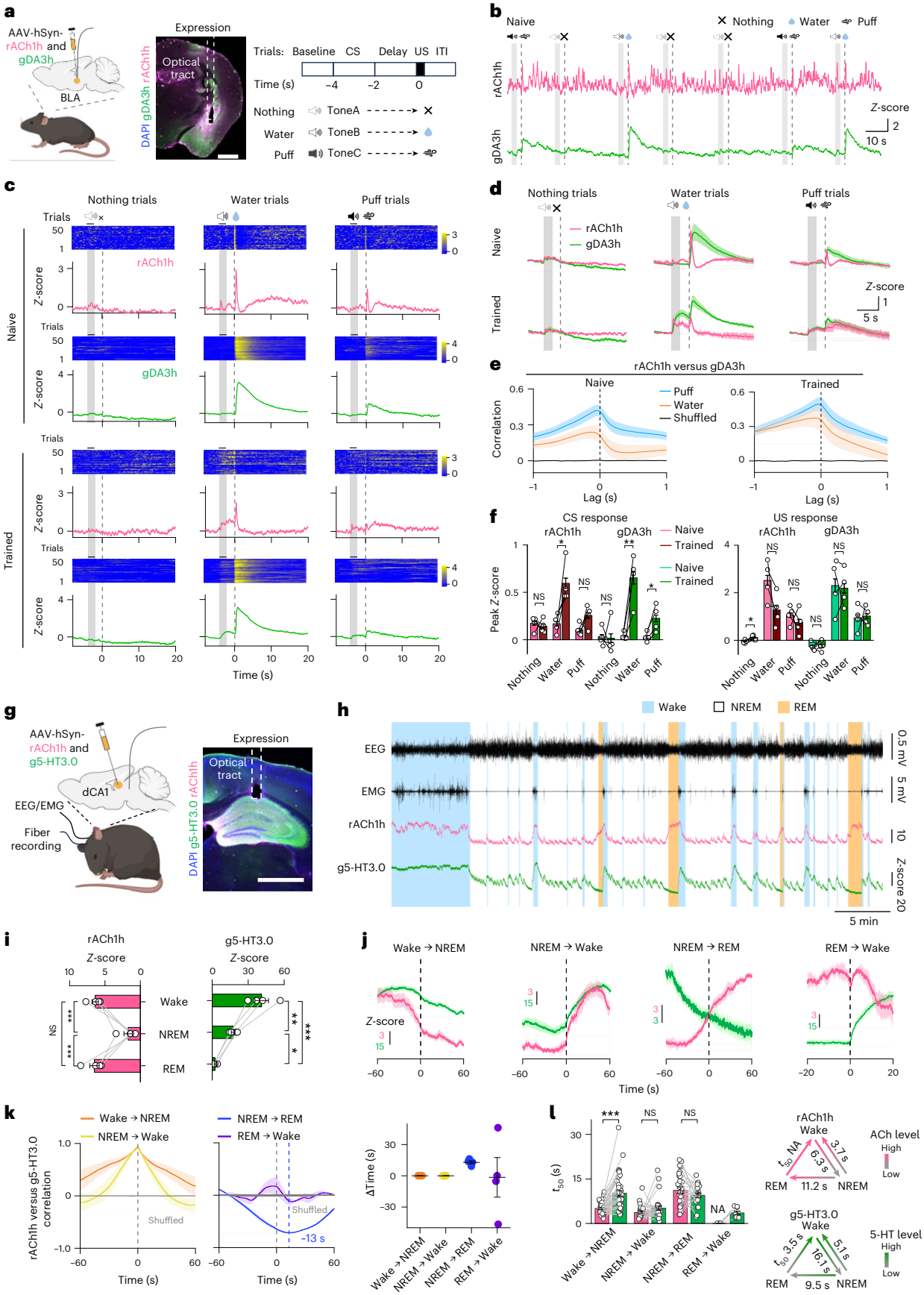

arousal, attention and motivation[6]. The noradrenergic neurons from the locus coeruleus broadly influence cortical activity[44,45]. To simultaneously measure ACh and NE release in the dorsal cortex, we coexpressed rACh1h and NE2m in the cortex for dual-color wide-field imaging[15,46] (Fig. 4a,b). After 2 weeks, we head-fixed the mice on a treadmill for imaging and applied distinct 5-s auditory cues during the mesoscopic imaging: wildcat (a wildcat meow), mating (a mating-related ultrasonic vocalization) and pain (a pain-associated ultrasonic vocalization). We aligned our imaging data to the Allen Common Coordinate Framework v3 (CCFv3) atlas[47]. Pseudocolor images and regional correlations revealed that the rACh1h sensor exhibited distinct dynamics in response to the auditory stimuli (Fig. 4c,d). Although both rACh1h and NE2m signals were responsive to the auditory stimuli, the rACh1h signal exhibited a particularly strong response in the somatosensory cortex during the pain vocalization (Fig. 4e–g). Control experiments confirmed the specificity of the ACh signal, as the response to the pain vocalization was abolished by the antagonist Scop (10 mg per kg) (Extended Data Fig. 8). We then analyzed the spatial distribution of the ACh and NE release during the pain vocalization (Fig. 4h). We found that the ACh release was predominantly localized to sensory cortical areas, whereas NE signals showed higher response in the motor cortex.

To test whether the rACh1h is able to multiplex two-photon imaging, we expressed both the red fluorescent rACh1h sensor and the green fluorescent NE2m sensor in the primary visual cortex (V1) (Extended Data Fig. 9a,b). During recording, the mouse was placed on a treadmill and was exposed to a variety of stimuli, including water delivery induced by licking, flashes of light, auditory tones and forced running (Extended Data Fig. 9c–f). We found that during water licking, rACh1h fluorescence increased, whereas NE2m fluorescence was unchanged. Moreover, forced running significantly increased both rACh1h and NE2m fluorescence, whereas visual and auditory stimuli produced no response in either sensor (Extended Data Fig. 9g,h). These results obtained with the rACh1h sensor are consistent with previous reports regarding the gACh3.0 signal measured in V1[18]. To validate the specificity of rACh1h signal, we expressed the rAChmut sensor with NE2m in the same region. The rAChmut sensor showed no significant response in both licking and running (Extended Data Fig. 10a–c). Then we analyzed the spatial distribution of the rACh1h and NE2m signals during water licking and forced running (Extended Data Fig. 9i–k). During licking, an increase in ACh release was observed in 4.8% of the total area imaged, with no change in NE release; during running, 4.7% of the total imaged area showed an increase in both ACh and NE release, and ACh release alone and NE release alone were observed in 24.1% and 4.3%, respectively, of the total imaged area. In summary, these findings demonstrate that rACh1h can be combined with NE2m to simultaneously record both ACh and NE release in the dorsal cortex.

Discussion

Here we developed a series of genetically encoded red fluorescent ACh sensors. We then demonstrated that these sensors can be used to monitor ACh dynamics both in vitro and in vivo with extremely high sensitivity and spatiotemporal resolution.

To maximize flexibility, we generated three versions of ACh sensors based on their ligand affinity, with rACh1h, rACh1m and rACh1l having high, medium and low affinity for ACh, respectively. These sensors—particularly rACh1h—exhibit a stronger response to ACh and a higher SNR compared to previously reported sensors, both in cultured cells and in cultured neurons.

The mApple-based red sensors may exhibit blue-light-induced photoswitching[48]. When red sensors are coexpressed with optogenetic proteins within the same brain region, blue-light stimulation can change their fluorescence, which may be misinterpreted as endogenous neurotransmitter dynamics[49,50]. Although rACh1h shows a largely attenuated photoswitching signal, its fluorescence signal still increases slightly under blue light excitation compared to rACh1l. Therefore, experiments combining rACh1h with optogenetics in the same brain region require extra caution to account for potential photoswitching interference.

During rACh1h characterization in acute brain slices, we observed that the rACh1h response began to decline before the 100-pulse stimulation ended (Fig. 2c). One possibility is the depletion of readily releasable ACh vesicles during the sustained stimulation[51]. Alternatively, given that the electrical stimulation is nonspecific, other neuromodulators in the NAc, such as γ-aminobutyric acid (GABA) and DA, might have regulated cholinergic neuron activity. The prior research indicated that cholinergic neurons in the NAc received local GABAergic input[52,53], and DA can inhibit ACh release through D2 receptors[11,12]. These interactions could collectively account for the observed decrease in rACh1h response during sustained electrical stimulation.

It is important to note that for the optoevoked ACh measurements (Fig. 2g,h and Extended Data Fig. 4a,b), we employed optogenetic stimulation in the BF of WT mice. The BF is known to contain GABAergic and glutamatergic populations[54,55]. Consequently, our optogenetic approach may have activated these cells, which could in turn modulate ACh release in the BLA or have independent downstream effects.

The red ACh sensors are developed from the muscarinic 3 receptor. To verify the ACh signal recorded by the rACh1h sensor, we applied three commonly used muscarinic receptor antagonists[56–58]—Tio, Scop and Trop—to block the signal as a control. Tio does not effectively cross the blood–brain barrier[59] and is therefore used in ex vivo acute brain-slice experiments. Scop and Trop are blood–brain barrier permeable and were used for in vivo fiber-photometry recordings and mesoscopic imaging.

Fig. 4 | Mesoscopic imaging of ACh and NE dynamics in the dorsal cortex. **a**, Schematic illustration and expression images of rACh1h and NE2m for mesoscopic imaging. The CCFv3 atlas was used for anatomical alignment. Scale bar: 1 mm. **b**, Schematic illustration depicting the 2-color mesoscopic imaging with auditory stimulation. **c**, Representative pseudocolor images (left) and normalized response along the anterior-to-posterior axis (right) of rACh1h and NE2m to auditory stimuli. Scale bar, 1 mm. **d**, Average peak correlation matrices of ACh and NE during auditory stimuli across CCFv3-defined cortical parcels. $n = 3$ mice. **e**, Representative heatmap of rACh1h and NE2m fluorescence responses in MOs, SSp-bfd, SSp-ll and VISp during auditory stimuli. **f**, Quantifications of peak $\Delta F/F_0$ in SSp-ll for rACh1h and NE2m during different auditory stimuli. Mean ± s.e.m. $n = 3$ mice. One-way ANOVA with post hoc Tukey's test was performed. For rACh1h, post hoc test: $P = 3.1 \times 10^{-5}$, 0.006 and 4.6×10^{-5} for pain versus no sound, wildcat and pain (Scop), respectively. **g**, Representative pseudocolor images (top) and traces (bottom) of rACh1h and NE2m responses during pain vocalization. The polygon outlines in the pseudocolor images enclose the region of interest (ROI) for response. Dashed lines indicate the timepoint of pseudocolor images. The pain vocalization data here come from the same mouse as shown in **c**. **h**, Pseudocolor images depicting the average peak increase of rACh1h (left) and NE2m (right) fluorescence measured during the pain vocalization. Middle: normalized peak responses measured in the indicated cortical structures. Mean ± s.e.m. $n = 3$ mice. One-way ANOVA with post hoc Tukey's test was performed. For rACh1h, post hoc test: $P = 0.046$, 0.036, 0.042 and 0.008 for SSp-ll versus SSp-bfd, VISrl, VISpm and VISp, respectively. For NE2m, post hoc test: $P = 0.011$, 0.005 and 0.034 for VISrl versus MOs, MOp and SSp-ul, respectively. A, anterior; MOp, primary motor area; MOs, secondary motor area; Mot, motor network; P, posterior; RS, retrosplenial network; RSPagl, retrosplenial area, lateral agranular part; RSPd, retrosplenial area, dorsal part; SS, somatosensory network; SSp-bfd, primary somatosensory area, barrel field; SSp-ll, primary somatosensory area, lower limb; SSp-ul, primary somatosensory area, upper limb; SSp-tr, primary somatosensory area, trunk; SSp-un, primary somatosensory area, unassigned; Vis, visual network; VISa, anterior visual area; VISam, anteromedial visual area; VISp, primary visual area; VISpm, posteromedial visual area; VISrl, rostrolateral visual area; RM, reflective mirror; DM, dichroic mirror. Panels **a**, **b**, **g** and **h** created in BioRender; Li, Y. https://biorender.com/xngrhc6 (2026).

https://doi.org/10.1038/s41593-026-02325-w

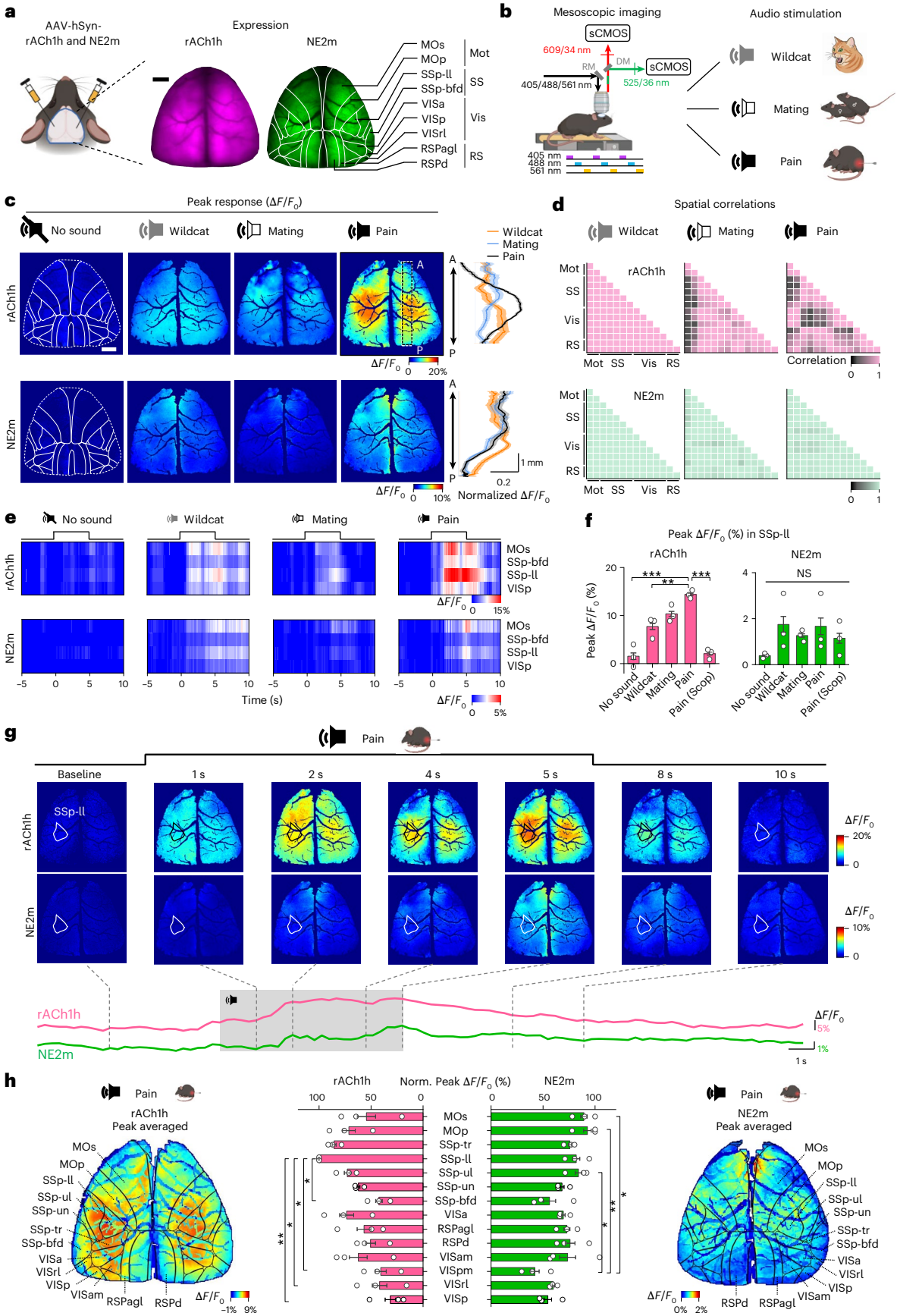

We showed that rACh1h is suitable for monitoring ACh release in brain areas that receiving cholinergic input, including the BLA, the CA1 region of the hippocampus and V1, as well as regions containing local cholinergic neurons such as the NAc. Importantly, the red-shifted spectrum of rACh1h allows for the simultaneous recording of ACh and a variety of other neurochemicals and signaling molecules, including calcium, DA, 5-HT and NE. Thus, by combining the rACh1h and g5-HT3.0 sensors, we found that ACh and 5-HT have similar oscillations during wakefulness and NREM sleep but have opposing activity patterns during REM sleep, suggesting that these two neuromodulators have distinct roles in the brain during various sleep–wake states.

In the control experiment of rAChmut in the sleep–wake cycle, the AChmut sensor showed a decreased signal during REM sleep (Extended Data Fig. 7b). This decrease may be caused by hemodynamic factors, as prior research has demonstrated sleep-cycle-dependent perivascular dynamics[60,61]. To mitigate these hemodynamic factors, a control experiment involving the administration of the muscarinic receptor antagonists can be employed (Fig. 2h and Extended Data Figs. 4b and 5f,g). The red ACh sensors showed no detectable response after the pharmacology treatment.

In summary, these red fluorescent ACh sensors significantly expand our ability to monitor ACh release with high sensitivity and spatiotemporal resolution. Moreover, their wide detection range and spectral compatibility with other fluorescent sensors provide a powerful set of tools for deciphering the complexity of the cholinergic system.

Online content

Any methods, additional references, Nature Portfolio reporting summaries, source data, extended data, supplementary information, acknowledgements, peer review information; details of author contributions and competing interests; and statements of data and code availability are available at https://doi.org/10.1038/s41593-026-02325-w.

References

1. Dale, H. H. The action of certain esters and ethers of choline, and their relation to muscarine. *J. Pharmacol. Exp. Ther.* **6**, 147–190 (1914).
2. Katz, B. & Miledi, R. The measurement of synaptic delay, and the time course of acetylcholine release at the neuromuscular junction. *Proc. R. Soc. Lond. B* **161**, 483–495 (1965).
3. Peper, K., Bradley, R. J. & Dreyer, F. The acetylcholine receptor at the neuromuscular junction. *Physiol. Rev.* **62**, 1271–1340 (1982).
4. Picciotto, M. R., Higley, M. J. & Mineur, Y. S. Acetylcholine as a neuromodulator: cholinergic signaling shapes nervous system function and behavior. *Neuron* **76**, 116–129 (2012).
5. Ballinger, E. C., Ananth, M., Talmage, D. A. & Role, L. W. Basal forebrain cholinergic circuits and signaling in cognition and cognitive decline. *Neuron* **91**, 1199–1218 (2016).
6. Ananth, M. R., Rajebhosale, P., Kim, R., Talmage, D. A. & Role, L. W. Basal forebrain cholinergic signalling: development, connectivity and roles in cognition. *Nat. Rev. Neurosci.* **24**, 1–19 (2023).
7. Jones, B. E. Arousal and sleep circuits. *Neuropsychopharmacol.* **45**, 6–20 (2020).
8. Xuan, F., Li, G., Li, Y. & Dombeck, D. A. Modulation of speed-dependent acetylcholine release in the hippocampus by spatial task engagement. *Cell Rep.* **44**, 116443 (2025).
9. Threlfell, S. et al. Striatal dopamine release is triggered by synchronized activity in cholinergic interneurons. *Neuron* **75**, 58–64 (2012).
10. Neyhart, E. et al. Cortical acetylcholine dynamics are predicted by cholinergic axon activity and behavior state. *Cell Rep.* **43**, 114808 (2024).
11. Chantranupong, L. et al. Dopamine and glutamate regulate striatal acetylcholine in decision-making. *Nature* **621**, 577–585 (2023).
12. Liu, C. et al. An action potential initiation mechanism in distal axons for the control of dopamine release. *Science* **375**, 1378–1385 (2022).
13. Krok, A. C. et al. Intrinsic dopamine and acetylcholine dynamics in the striatum of mice. *Nature* **621**, 543–549 (2023).
14. Zhang, Y. et al. Interaction of acetylcholine and oxytocin neuromodulation in the hippocampus. *Neuron* **112**, 1862–1875 (2024).
15. Lohani, S. et al. Spatiotemporally heterogeneous coordination of cholinergic and neocortical activity. *Nat. Neurosci.* **25**, 1706–1713 (2022).
16. Hampel, H. et al. The cholinergic system in the pathophysiology and treatment of alzheimer's disease. *Brain* **141**, 1917–1933 (2018).
17. Jing, M. et al. A genetically encoded fluorescent acetylcholine indicator for in vitro and in vivo studies. *Nat. Biotechnol.* **36**, 726–737 (2018).
18. Jing, M. et al. An optimized acetylcholine sensor for monitoring in vivo cholinergic activity. *Nat. Methods* **17**, 1139–1146 (2020).
19. Borden, P. M. et al. A fast genetically encoded fluorescent sensor for faithful in vivo acetylcholine detection in mice, fish, worms and flies. Preprint at *bioRxiv* https://doi.org/10.1101/2020.02.07.939504 (2020).
20. Sun, F. et al. Next-generation GRAB sensors for monitoring dopaminergic activity in vivo. *Nat. Methods* **17**, 1156–1166 (2020).
21. Zhuo, Y. et al. Improved green and red GRAB sensors for monitoring dopaminergic activity in vivo. *Nat. Methods* **21**, 680–691 (2024).
22. Deng, F. et al. Improved green and red GRAB sensors for monitoring spatiotemporal serotonin release in vivo. *Nat. Methods* **21**, 692–702 (2024).
23. Ballesteros, J. A. & Weinstein, H. in *Methods in Neurosciences*, Vol. 25 (ed. Sealfon, S. C.) Ch. 19 (Academic, 1995).
24. Soreq, H. & Seidman, S. Acetylcholinesterase—new roles for an old actor. *Nat. Rev. Neurosci.* **2**, 294–302 (2001).
25. Patriarchi, T. et al. An expanded palette of dopamine sensors for multiplex imaging in vivo. *Nat. Methods* **17**, 1147–1155 (2020).
26. Dana, H. et al. Sensitive red protein calcium indicators for imaging neural activity. *eLife* **5**, e12727 (2016).
27. Wu, J. et al. Improved orange and red Ca^{2+} indicators and photophysical considerations for optogenetic applications. *ACS Chem. Neurosci.* **4**, 963–972 (2013).
28. Wan, Q. et al. Mini G protein probes for active G protein–coupled receptors (GPCRs) in live cells. *J. Biol. Chem.* **293**, 7466–7473 (2018).
29. Kroeze, W. K. et al. PRESTO-tango as an open-source resource for interrogation of the druggable human GPCRome. *Nat. Struct. Mol. Biol.* **22**, 362–369 (2015).
30. Zhou, F.-M., Liang, Y. & Dani, J. A. Endogenous nicotinic cholinergic activity regulates dopamine release in the striatum. *Nat. Neurosci.* **4**, 1224–1229 (2001).
31. Ryan, T. A., Reuter, H. & Smith, S. J. Optical detection of a quantal presynaptic membrane turnover. *Nature* **388**, 478–482 (1997).
32. Ariel, P. & Ryan, T. A. Optical mapping of release properties in synapses. *Front. Neural Circuits* **4**, 18 (2010).
33. Sun, F. et al. A genetically encoded fluorescent sensor enables rapid and specific detection of dopamine in flies, fish, and mice. *Cell* **174**, 481–496 (2018).
34. Crouse, R. B. et al. Acetylcholine is released in the basolateral amygdala in response to predictors of reward and enhances the learning of cue-reward contingency. *eLife* **9**, e57335 (2020).
35. Nagel, G. et al. Channelrhodopsin-2, a directly light-gated cation-selective membrane channel. *Proc. Natl Acad. Sci. USA* **100**, 13940–13945 (2003).

36. Zemek, F. et al. Outcomes of alzheimer's disease therapy with acetylcholinesterase inhibitors and memantine. *Expert Opin. Drug Saf.* **13**, 759–774 (2014).
37. English, D. F. et al. GABAergic circuits mediate the reinforcement-related signals of striatal cholinergic interneurons. *Nat. Neurosci.* **15**, 123–130 (2012).
38. Gritton, H. J. et al. Unique contributions of parvalbumin and cholinergic interneurons in organizing striatal networks during movement. *Nat. Neurosci.* **22**, 586–597 (2019).
39. Hasselmo, M. E. The role of acetylcholine in learning and memory. *Curr. Opin. Neurobiol.* **16**, 710–715 (2006).
40. Baxter, M. G. & Murray, E. A. The amygdala and reward. *Nat. Rev. Neurosci.* **3**, 563–573 (2002).
41. Schultz, W., Dayan, P. & Montague, P. R. A neural substrate of prediction and reward. *Science* **275**, 1593–1599 (1997).
42. Payne, J. D. & Nadel, L. Sleep, dreams, and memory consolidation: the role of the stress hormone cortisol. *Learn. Mem.* **11**, 671–678 (2004).
43. Wan, J. et al. A genetically encoded sensor for measuring serotonin dynamics. *Nat. Neurosci.* **24**, 746–752 (2021).
44. Schwarz, L. A. & Luo, L. Organization of the locus coeruleus-norepinephrine system. *Curr. Biol.* **25**, R1051–R1056 (2015).
45. Schwarz, L. A. et al. Viral-genetic tracing of the input–output organization of a central noradrenaline circuit. *Nature* **524**, 88–92 (2015).
46. Feng, J. et al. Monitoring norepinephrine release in vivo using next-generation GRABNE sensors. *Neuron* **112**, 1930–1942 (2024).
47. Wang, Q. et al. The allen mouse brain common coordinate framework: a 3D reference atlas. *Cell* **181**, 936–953 (2020).
48. Shaner, N. C. et al. Improving the photostability of bright monomeric orange and red fluorescent proteins. *Nat. Methods* **5**, 545–551 (2008).
49. Taniguchi, J. et al. Comment on 'accumbens cholinergic interneurons dynamically promote dopamine release and enable motivation. *eLife* **13**, e95694 (2024).
50. Mohebi, A., Collins, V. L. & Berke, J. D. Accumbens cholinergic interneurons dynamically promote dopamine release and enable motivation. *eLife* **12**, e85011 (2023).
51. Alabi, A. A. & Tsien, R. W. Synaptic vesicle pools and dynamics. *Cold Spring Harb. Perspect. Biol.* **4**, a013680 (2012).
52. Sato, A., Sasaoka, T., Nishijo, T. & Momiyama, T. GABAergic synaptic transmission onto striatal cholinergic interneurons in dopamine D2 receptor knock-out mice. *Neuroscience* **263**, 138–147 (2014).
53. Brown, M. T. C. et al. Ventral tegmental area GABA projections pause accumbal cholinergic interneurons to enhance associative learning. *Nature* **492**, 452–456 (2012).
54. Xu, M. et al. Basal forebrain circuit for sleep-wake control. *Nat. Neurosci.* **18**, 1641–1647 (2015).
55. Do, J. P. et al. Cell type-specific long-range connections of basal forebrain circuit. *eLife* **5**, e13214 (2016).
56. Disse, B. et al. Ba 679 BR, a novel long-acting anticholinergic bronchodilator. *Life Sci.* **52**, 537–544 (1993).
57. Klinkenberg, I. & Blokland, A. The validity of scopolamine as a pharmacological model for cognitive impairment: a review of animal behavioral studies. *Neurosci. Biobehav. Rev.* **34**, 1307–1350 (2010).
58. Lazareno, S., Buckley, N. J. & Roberts, F. F. Characterization of muscarinic M4 binding sites in rabbit lung, chicken heart, and NG108-15 cells. *Mol. Pharmacol.* **38**, 805–815 (1990).
59. Heredia, J. L. Tiotropium bromide: an update. *Open Respir. Med. J.* **3**, 43–52 (2009).
60. Bojarskaite, L. et al. Sleep cycle-dependent vascular dynamics in male mice and the predicted effects on perivascular cerebrospinal fluid flow and solute transport. *Nat. Commun.* **14**, 953 (2023).
61. Hauglund, N. L. et al. Norepinephrine-mediated slow vasomotion drives glymphatic clearance during sleep. *Cell* **188**, 606–622 (2025).
62. Abramson, J. et al. Accurate structure prediction of biomolecular interactions with AlphaFold 3. *Nature* **630**, 493–500 (2024).

https://doi.org/10.1038/s41593-026-02325-w

Methods

Animals

All animal studies and experimental procedures were approved by the laboratory animal care and use committee of Peking University. Newborn WT Sprague–Dawley rat pups (P0) and WT male C57BL/6 J mice (8–12 weeks old, from Beijing Vital River Laboratory) were used in this study. D1R-Cre mice were generously provided by Y. Rao at Peking University. ChAT-Cre mice were generously provided by M. Luo at Chinese Institute for Brain Research. All animals were group-housed or pair-housed at 18–23 °C in 40–60% humidity, with a 12 h/12 h light/dark cycle and food and water provided ad libitum.

AAV expression

AAV2/9-hSyn-rACh1h (9.63×10^{13} vg ml^{-1}), AAV2/9-EF1a-DIO-rACh1h (7.30×10^{13} vg ml^{-1}), AAV2/9-hSyn-rAChmut (3.86×10^{13} vg ml^{-1}), AAV2/9-hSyn-rACh1m (4.40×10^{13} vg ml^{-1}), AAV2/9-hSyn-rACh1l (1.03×10^{13} vg ml^{-1}), AAV2/9-hSyn-gACh3.0 (8.0×10^{13} vg ml^{-1}), AAV2/9-hSyn-gDA3h (8.43×10^{13} vg ml^{-1}), AAV2/9-hSyn-g5-HT3.0 (1.66×10^{13} vg ml^{-1}) and AAV2/9-hSyn-iAChSnFR (3.53×10^{13} vg ml^{-1}) were packaged at Vigene Biosciences. AAV2/9-hSyn-hChR2(H134R)-eYFP (5.49×10^{12} vg ml^{-1}) and AAV2/9-hSyn-DIO-GCaMP6s (5.52×10^{12} vg ml^{-1}) were packaged at BrainVTA. AAV2/9-hSyn-NE2m (1.39×10^{13} vg ml^{-1}) was packaged at Shenzhen Bay Laboratory. Where indicated, the AAVs were either used to infect cultured neurons or injected in vivo into specific brain regions.

Molecular biology

All plasmids used in this study were generated using Gibson assembly[63], and the sequences of all clones were confirmed using Sanger sequencing. cDNAs encoding muscarinic type 3 receptors were cloned from a mouse cDNA library and a human G-protein-coupled receptor cDNA library (hORFeome database 8.1, http://horfdb.dfci.harvard.edu/index.php?page=home). To screen and characterize the sensors in HEK293T cells, the sensor-encoding cDNAs were cloned into the pDisplay vector containing an upstream IgK leader sequence and a downstream IRES-EGFP-CAAX cassette. The EGFP-CAAX cassette provides a membrane marker and was used to calibrate fluorescence. To optimize the sensors, site-directed mutagenesis was performed using primers containing randomized NNB codons (48 codons in total, encoding all 20 possible amino acids). For expression and characterization in cultured neurons, the sensors were cloned into the pAAV vector containing the human Synapsin promoter. To measure downstream coupling using the Tango assay, the indicated rACh sensor or WT M_3R was cloned into the pTango vector[29]. For the luciferase complementation assay, the *β2AR* gene in the β2AR-SmBiT construct was replaced with the indicated rACh sensor or WT M_3R; LgBiT-mGs was a gift from N. A. Lambert (Augusta University).

Cell culture

HEK293T cells were purchased from ATCC (CRL-3216). The cells were cultured at 37 °C in humidified air containing 5% CO_2 in Dulbecco's Modified Eagle's Medium (Biological Industries) supplemented with 10% (v/v) fetal bovine serum (Gibco) and 1% penicillin–streptomycin (Gibco). Rat cortical neurons were prepared using P0 Sprague–Dawley rat pups (both sexes) purchased from Beijing Vital River. Rat cortical neurons were dissociated from the dissected rat cerebral cortex by digestion in 0.25% trypsin-EDTA (Biological Industries) and plated on poly-D-lysine–coated (Sigma-Aldrich) 12-mm glass coverslips in 24-well plates. The neurons were cultured in neurobasal medium (Gibco) containing 2% B-27 supplement (Gibco), 1% GlutaMAX (Gibco) and 1% penicillin–streptomycin (Gibco) at 37 °C in humidified air containing 5% CO_2.

Fluorescence imaging of cultured cells

HEK293T cells were cultured on 12-mm glass coverslips in 24-well plates or in 96-well plates without coverslips. When the cells reached ~70% confluence, they were transfected using polyethylenimine (PEI; 1 μg plasmid and 3 μg PEI per well in 24-well plates or 300 ng plasmid and 900 ng PEI per well in 96-well plates). Imaging was performed 24–48 h after transfection. For cortical neurons, the cells were infected with AAV expressing the indicated red fluorescent ACh sensor at 3–5 days in vitro and imaged at 11–14 days in vitro. Before imaging, the culture medium was replaced with Tyrode's solution consisting of (in mM) 150 NaCl, 4 KCl, 2 $MgCl_2$, 2 $CaCl_2$, 10 HEPES and 10 glucose (pH 7.4). For Fig. 1c,d, the cells grown on coverslips were transferred to a custom-made chamber and imaged using an inverted Ti-E A1RS+ confocal microscope (Nikon) with NIS-Element 4.51.00 software (Nikon). Images were acquired using a ×40/1.35 NA oil-immersion objective. A 488-nm laser with a 534/55-nm filter was used for green sensors, and a 561-nm laser with a 597/58-nm filter was used for red sensors. The cells cultured in 96-well plates without coverslips were imaged using an Opera Phenix system equipped with a ×20/0.4 numerical aperture (NA) objective, a ×40/1.1 NA water-immersion objective, a 488-nm laser and a 561-nm laser, controlled using Harmony 4.9 software.

To measure the sensors' responses induced by various chemicals, solutions containing the following compounds were delivered to the cells by bath application or perfusion at the indicated concentrations: ACh (AMQUAR), Tio (MCE), Scop (MCE), choline (Sigma-Aldrich), nicotine (Tocris), Glu (Sigma-Aldrich), GABA (Tocris), DA (Sigma-Aldrich), NE (Tocris), 5-HT (Tocris), histamine (Tocris), octopamine (Tocris), tyramine (Aladdin) and adenosine (Sigma-Aldrich). The change in fluorescence ($\Delta F/F_0$) was measured using the formula $[(F - F_0)/F_0]$, in which F_0 is baseline fluorescence defined as the average fluorescence measured 0–1 min before drug application.

In the experiment to test whether blue light can photoswitch the red fluorescent sensors, cells expressing the indicated rACh sensors or jRGECO1a were imaged using an inverted Ti-E A1 confocal microscope, and the cells were stimulated with a 488-nm laser emitted from the objective (power: 210 μW; intensity: 0.4 W cm^{-2}). The laser was applied for a duration of 1 s.

Spectra measurements

To measure one-photon spectra, HEK293T cells were transfected with plasmids encoding the various rACh sensors and then transferred to 384-well plates 24–30 h after transfection. The excitation and emission spectra were then measured at 5-nm increments using a Safire2 multimode plate reader (Tecan) in the absence and presence of 100-μM ACh. To measure two-photon spectra, HEK293T cells were plated on 12-mm coverslips and transfected with plasmid encoding the various rACh sensors, and excitation spectra were measured at 10-nm increments ranging from 820 nm to 1,300 nm using an FVMPE-RS microscope (Olympus) equipped with a Spectra-Physics InSight X3 dual-output laser.

Luciferase complementation assay

HEK293T cells at 50–60% confluence were cotransfected with either WT M_3R or the indicated sensor together with the corresponding LgBiT-mG construct; 24–48 h post-transfection, the cells were washed in phosphate-buffered saline (PBS), dissociated using a cell scraper and resuspended in PBS. The cells were then transferred to opaque 96-well plates containing 5-μM furimazine (NanoLuc Luciferase Assay, Promega) and bathed in ACh at concentrations ranging from 0.1 nM to 100 μM. After incubation for 10 min in the dark, luminescence was measured using a VICTOR X5 multilabel plate reader (PerkinElmer).

Tango assay

The Tango assay was performed using the HTLA cell line, which stably expresses a tTA-dependent luciferase reporter alongside a β-arrestin2-TEV fusion gene. These cells were transfected with plasmids encoding the indicated receptors or sensors. After culturing for 24 h in six-well plates, the cells were transferred to 96-well plates and bathed

in ACh at concentrations ranging from 0.01 nM to 100 µM. After a 12-h incubation to facilitate expression of the tTA-dependent luciferase, the Bright-Glo reagent (Fluc Luciferase Assay System, Promega) was added to a final concentration of 5 µM, and luminescence was measured using a VICTOR X5 multilabel plate reader (PerkinElmer).

Two-photon imaging of acute mouse brain slices

WT adult (6–8 weeks of age) male C57BL/6 J mice were anesthetized with an i.p. injection of 2,2,2-tribromoethanol (Avertin, 500 mg per kg body weight; Sigma-Aldrich), and AAV-hSyn-rACh1h was injected (300 nl at a rate of 50 nl min^{-1}) into the NAc using the following coordinates: anterior–posterior (AP): +1.4 mm relative to Bregma; medial–lateral (ML): ±1.2 mm relative to Bregma; and dorsal–ventral (DV): −4.0 mm from the dura. For the experiment depicted in Extended Data Fig. 3a, we specifically used Chat-cre mice and injected AAV-EF1a-DIO-rACh1h (300 nl at 50 nl min^{-1}) into the NAc at the previously mentioned coordinates. Three weeks after virus injection, the mice were deeply anesthetized, and the heart was perfused with slicing buffer containing (in mM) 110 choline chloride, 2.5 KCl, 1.25 NaH_2PO_4, 25 $NaHCO_3$, 7 $MgCl_2$, 25 glucose and 0.5 $CaCl_2$. The mice were then decapitated, and the brains were immediately removed and placed in cold oxygenated slicing buffer. The brains were sectioned into 300-µm-thick coronal slices using a VT1200 vibratome (Leica), and the slices were incubated at 34 °C for at least 40 min in oxygenated artificial cerebrospinal fluid containing (in mM) 125 NaCl, 2.5 KCl, 1 NaH_2PO_4, 25 $NaHCO_3$, 1.3 $MgCl_2$, 25 glucose and 2 $CaCl_2$. Two-photon imaging was performed using an Ultima Investigator two-photon microscope (Bruker) equipped with a ×20/1.00 NA objective (Olympus) and an InSight X3 tunable laser (Spectra-Physics), using Prairie View 5.5 software (Bruker). A 1,040-nm laser was used to excite the rACh1h sensor, and a 595/50-nm emission filter was used to collect the fluorescence signal. For electrical stimulation, a bipolar electrode (model WE30031.0A3, MicroProbes) was positioned near the NAc core under fluorescence guidance, and imaging and stimulation were synchronized using an Arduino board with custom-written software; the stimulation voltage was set at 4–5 V. Where indicated, compounds were added by perfusion at a flow rate of 4 ml min^{-1}.

Fiber photometry recording of optogenetically induced ACh release in mice

Adult male C57BL/6 J mice, aged 8–9 weeks, were used in this study. They were anesthetized using 1.5% isoflurane and secured in a stereotaxic apparatus to ensure precise targeting during the procedure. AAV-hSyn-rACh1h, AAV-hSyn-rACh1m, AAV-hSyn-rACh1l or AAV-hSyn-rAChmut (300 nl) was injected into the BLA using the following coordinates: AP: −1.4 mm relative to Bregma; ML: ±3.0 mm relative to Bregma; and DV: −4.0 mm from the dura. For activation of the BF, AAV-hSyn-ChR2-YFP (300 nl) was injected into the BF using the following coordinates: AP: 0 mm relative to Bregma; ML: ±1.5 mm relative to Bregma; and DV: −4.8 mm from the dura. Two optical fibers (200-µm diameter, 0.37 NA; Inper) were implanted; one optical fiber was positioned 0.1 mm above the virus injection site in the BLA to record the ACh sensor, and the other optical fiber was positioned 0.3 mm above the virus injection site in the BF to optically activate ChR2. The optical fibers were secured to the skull surface using dental cement (3M).

Two to three weeks after virus injection, fluorescence signals were recorded using a fiber photometry system (FPS-410/470/561; Inper). Yellow LED light was bandpass-filtered (561/10 nm), reflected by a dichroic mirror (495 nm) and then focused using a ×20 objective (Olympus). An optical fiber was used to guide the light between the commutator and the implanted optical fiber cannulas. The excitation light emitted by the LED was set to 20–30 µW and delivered at 10 Hz with a 10-ms pulse duration. The optical signals were then collected through the optical fibers. Red fluorescence was bandpass-filtered (520/20 nm and 595/30 nm) and captured using a scientific complementary metal–oxide–semiconductor (sCMOS) camera. The current output generated by the photomultiplier tube was transduced into a voltage signal using an amplifier (A-M Systems) and subsequently passed through a low-pass filter to remove high-frequency noise. The analog voltage signals were then digitized using an acquisition card (National Instruments). To reduce autofluorescence generated by the optical fibers, the recording fibers were photobleached using a high-power LED before recording. Background autofluorescence was recorded and subtracted from the recorded signals in the subsequent analysis. A 488-nm laser (1–160 mW, LL-laser) was used for optical stimulation, with the light power at the fiber tip set at 10 mW. Optical stimuli were delivered at 40 pulses with 10-ms duration for 1 s concurrently with photometry recording. Where indicated, the mice received an i.p. injection of Done (3 mg per kg body weight) followed by an i.p. injection of Scop (10 mg per kg body weight).

In the fiber photometry experiments, data were first processed using Spike2 8.18 software. To correct for photobleaching of fluorescence signals (baseline drift), we used a biexponential curve to the raw fluorescence trace and subtracted as follows:

$$\text{Fraw fit} = \text{fit(Fraw, 'exp 2')}$$

$$\text{Fraw correction} = \text{Fraw} - \text{Fraw fit}$$

The photometry data were then analyzed using a custom-written MATLAB program (MATLAB R2022a, MathWorks). To calculate $\Delta F/F_0$, baseline fluorescence (F_0) was defined as the average fluorescence measured 5 s before the five trials of optical stimulation under control conditions.

Dual-color recording of calcium and rACh1h in the NAc

Adult male and female D1R-Cre mice (10–14 weeks old) were used for this experiment. AAV9-hsyn-rACh1h and AAV9-hsyn-DIO-GCaMP6s (1:1 mix, 500 nl total volume) was unilaterally injected into the NAc (AP: +1.4 mm relative to Bregma; ML: ±1.2 mm relative to Bregma; and DV: −4.0 mm from the dura), and an optical fiber (200-µm diameter, 0.37 NA; Inper) was implanted 0.1 mm above the virus injection site. For the experiments shown in Extended Data Fig. 5h, a combination of AAV-hSyn-rAChmut and AAV9-hsyn-DIO-GCaMP6s was injected into the NAc using the coordinates indicated above. Photometry recording was performed 2–3 weeks after virus injection using a customized three-color photometry system (Thinker Tech). A 470/10-nm (model 65144; Edmund optics) filtered LED at 40 µW was used to excite the green fluorescent sensors, and a 555/20-nm (model ET555/20x; Chroma) filtered LED at 40 µW was used to excite the red fluorescent sensors. The excitation lights were delivered sequentially at 20 Hz with a 10-ms pulse duration for each, and fluorescence was collected using an sCMOS camera (Tucsen) and filtered with a three-bandpass filter (model ZET405/470/555/640m; Chroma). To minimize autofluorescence from the optical fiber, the recording fiber was photobleached using a high-power LED before recording.

An intraoral cheek fistula was implanted in each mouse for sucrose delivery. Incisions were made in the cheek and the scalp at the back of the neck. A short, soft silastic tube (inner diameter: 0.3 mm; outer diameter: 0.7 mm) connected via an L-shaped stainless-steel tube was then inserted into the cheek incision site. The steel tube was routed through the scalp incision, with the opposite end inserted into the oral cavity. After 3 days of recovery from the surgery, the mice were water-restricted for 36 h (until reaching 85% of their initial body weight). The water-restricted, freely moving mice then received 5% sucrose water delivery (approximately 8 µl per trial, with 25–50 trials per session and a trial interval of 20–30 s).

Before foot shock, the mice were placed in a shock box and habituated for 30 min. During the experiment, 10 1-s pulses of electricity were delivered at 0.7 mA, with an interval of 90–120 s between trials. Where

indicated, the mice received an i.p. injection of Trop (10 mg per kg body weight). The standard deviation (from −6 s to −3 s baseline of rACh1h) was used to calculate the *Z*-score.

Pavlovian auditory conditioning task

Adult (8–9 weeks of age) male C57BL/6 J mice were used for these experiments. A mixture of AAV-hSyn-rACh1h (200 nl) and AAV-hysn-gDA3h (200 nl) was injected into the right BLA as described above. An optical fiber cannula (Inper) was then implanted 0.1 mm above the virus injection site in the BLA to record the ACh and DA signals. For the experiments shown in Extended Data Fig. 6, a combination of AAV-hSyn-rAChmut and AAV-hSyn-gDA3h was injected into the BLA using the coordinates indicated above. A stainless-steel head holder was attached to the skull using resin cement to head-fix the animal. An intraoral cheek fistula was then implanted in each mouse for water delivery as described above. Head-fixed mice were habituated to the treadmill apparatus for 2 days (1 h per day) before the experiments to minimize stress. The mice were water-restricted for 36 h (until reaching 85% of their initial body weight). On the day of the experiment, the Pavlovian auditory conditioning task was performed using three pairs of auditory cues and outcomes: tone A (2.5 kHz, 70 dB, 2-s duration) was paired with delivery of 10 µl of 5% sucrose water; tone B (15 kHz, 70 dB, 2-s duration) was paired with delivery of an air puff to the eye; and tone C (7.5 kHz, 70 dB, 2-s duration) was paired with no delivery. These three pairs were randomly delivered for a total of 300 trials, with a 20-s to 30-s intertrial interval. The delivery of water and air puffs was precisely controlled by a stepper motor pump and solenoid valve, respectively. A custom-written Arduino code was used to control the timing of the pump and solenoid valve and to synchronize the training devices with the photometry recording system.

Two weeks after virus injection, the same fiber photometry system (Inper) was used to capture the fluorescence signals. In brief, a 10-Hz (10-ms pulse duration) 470/10-nm filtered LED at 20–30 µW was used to excite the green fluorescent sensors, and a 10-Hz (10-ms pulse duration) 561/10-nm filtered LED at 20–30 µW was used to excite the red fluorescent sensors. Alternating excitation wavelengths were delivered, and fluorescence signals were collected using a sCMOS camera during dual-color imaging. To calculate $\Delta F/F_0$, baseline fluorescence (F_0) was defined as the average fluorescence signal measured 4.5–5.0 s before the first auditory cue.

Fiber photometry recordings and polysomnographic recordings during the sleep–wake cycle

Adult WT C57BL/6 J mice were anesthetized with isoflurane and placed on a stereotaxic frame for AAV injection (400 nl per site). For the experiments shown in Fig. 3g, a combination of AAV-hSyn-rACh1h and AAV-hSyn-g5-HT3.0 was injected into the dCA1 using the following coordinates: AP: −2.0 mm relative to Bregma; ML: ±1.5 mm relative to Bregma; and DV: −1.4 mm from the dura. For the experiments shown in Extended Data Fig. 7, a combination of AAV-hSyn-rAChmut and AAV-hSyn-g5-HT3.0 was injected into the dCA1 using the coordinates indicated above. An optical fiber cannula (200-µm diameter, 0.37 NA; Inper) was placed 0.1 mm above the virus injection site to record the sensor signals and was affixed to the skull using dental cement.

To monitor the animal's sleep–wake state, custom-made EEG and EMG electrodes were attached and affixed to the skull via a microconnector. The EEG electrodes were implanted into craniotomy holes positioned above the frontal cortex and visual cortex, and the EMG wires were placed bilaterally in the neck musculature. The microconnector was attached securely to the skull using glue and a thick layer of dental cement. After surgery, the mice were allowed to recover for at least 2 weeks.

The same fiber photometry system (Inper) was used to record the fluorescence signals in freely moving mice during the sleep–wake cycle. For the experiments shown in Fig. 3g,h and Extended Data Fig. 7a–c, a 10-Hz 470/10-nm filtered light (20–30 µW) was used to excite the green fluorescent 5-HT sensor, and a 561/10-nm filtered light (20–30 µW) was used to excite the red fluorescent ACh sensors. The fluorescent signals were captured using a dual-band bandpass filter (520/20 nm and 595/30 nm), with 10-ms pulses of excitation light delivered at 10 Hz.

The photometry data were analyzed using a custom MATLAB program. To calculate $\Delta F/F_0$ during the sleep–wake cycle, baseline values of the ACh signal were measured during NREM sleep, and baseline values of the 5-HT signal were measured during REM sleep. To compare the change in fluorescence between animals, $\Delta F/F_0$ was divided by the standard deviation of the baseline signal to obtain a *Z*-score.

Mesoscopic in vivo imaging in mice

Adult (6–8 weeks of age) male C57BL/6 J mice were anesthetized with an i.p. injection of 2,2,2-tribromoethanol (Avertin, 500 mg per kg body weight; Sigma-Aldrich) and maintained with 1% isoflurane. The mouse was then fixed in a stereotaxic frame. The scalp and underlying muscles were carefully removed to expose the skull, and the majority of the skull above the dorsal cortex was removed. A 1:1 mixture of AAV-hSyn-rACh1h and AAV-hSyn-NE2m (diluted to ~1×10^{13} vg ml^{-1}) was injected into the dorsal cortex at 22–26 sites with 0.7-mm intervals (100 nl per site). After the injections, the cortex was covered with a custom-made coverslip to create an optical window, and a stainless-steel head holder was attached to the skull. The mice were given at least 14 days to recover, followed by an additional 3 days to habituate to the head fixation before imaging.

Mesoscopic imaging was performed using a customized dual-color macroscope equipped with a ×2/0.5 NA objective lens (Olympus, MVPLAPO2XC), two 1×/0.25 NA tube lenses (Olympus, MVPLAPO1X) and two sCMOS cameras (Andor, Zyla 4.2 Plus, 2,048 × 2,048 pixels, 16-bit). A multiline fiber-coupled laser system (Changchun New Industries Optoelectronics Tech. Co., Ltd., RGB-405/488/561/642nm -220mW-CC32594) generated three excitation wavelengths (405 nm, 488 nm and 561 nm). Emission light was passed through a long-pass dichroic mirror (Thorlabs, DMLP567L) and either a 525/36-nm or 609/34-nm emission filter (Chroma) and captured by the sCMOS cameras. Both the excitation laser and the camera exposure were triggered by an Arduino board (Uno) using custom-written programs. Dual-color imaging was performed using alternating illumination between the 405-nm laser and the 488-nm or/and 561-nm laser. Images were acquired using Micro-Manager 2.0 at 512-pixel × 512-pixel resolution at a rate of 5 Hz with 40-ms exposure. During imaging, the mice were head-fixed but could run freely on a linear treadmill. For auditory stimulation, 5 s of 70-dB auditory stimuli was generated using a RZ6 Multi I/O Processor (Tucker-Davis Technologies) and delivered via a magnetic speaker.

Analysis of mesoscopic imaging data

The raw images acquired from each camera were calibrated to ensure uniformity across the imaging region, and movement-related artifacts were corrected using the motion-correction algorithm NoRMCorre[64]. The corrected image stack with a size of 512 pixels × 512 pixels was downsampled by a factor of 0.5 to 256 × 256 pixels for further analysis. For dual-color imaging, the red-channel images were registered to the green-channel images by performing an automated transformation using the 'similarity' mode of the MATLAB function 'imregtform'. The same transformation was then applied to all red-channel images to align them with their corresponding green-channel images. The resulting image stack was saved as a binary file to facilitate the input and output of large files. A mask was created to exclude background and blood vessel pixels from the corrected image stack using the machine learning-based ImageJ plugin Trainable Weka Segmentation (v3.3.2); these minimized artifacts caused by blood vessel constriction and dilation. To correct the effects of hemodynamics on fluorescence[15,65], we performed a pixel-by-pixel correction based on a linear regression

of the ligand-dependent signals (excited by 488-nm or 561-nm light) against the ligand-independent signals (excited by 405-nm light) for both NE2m and rACh1h based on their respective spectra.

Baseline images were smoothed using a Gaussian filter ($\sigma = 2$), and linear regression was performed for each pixel by regressing the baseline fluorescence intensity (FI) of the 405-nm-excited channel onto the 488-nm or 561-nm signal. The regression coefficient was then used to rescale the 405-nm channel, which was then subtracted from the 488-nm or 561-nm signal. The corrected signal was added to the averaged rescaled 405-nm channel signal to avoid negative values. The response of each pixel was calculated using the following equation: $\Delta F/F_0 = (F - F_0) / F_0$, where F_0 is defined as the average baseline FI.

We registered the mean fluorescence image to a two-dimensional projection of the CCFv3 using four manually identified anatomical landmarks, including the left, center and right points in the boundary between the anterior cortex and the olfactory bulbs and the medial point at the base of the retrosplenial cortex. To analyze the time course of the response in a specific brain region, we calculated the average $\Delta F/F_0$ value for all available pixels within that region. To align and average the responses across the entire cortex from multiple mice, we developed a custom script to first register the peak response image for each individual mouse to the Allen CCFv3 and then averaged the images, preserving only the intersection pixels.

Two-photon in vivo imaging in mice

Adult (6–8 weeks of age) male C57BL/6 J mice were anesthetized with an i.p. injection of 2,2,2-tribromoethanol (Avertin, 500 mg per kg body weight; Sigma-Aldrich), the scalp was retracted, and the skull above V1 was removed. A mixture of AAVs expressing rACh1h and NE2m (1:1 mixture, 300 nl total volume, full titer) was injected into V1 using the following coordinates: AP: −2.5 mm relative to Bregma; ML: 2.2 mm relative to Bregma; and DV: −0.5 mm from the dura. A 3.0-mm diameter round coverslip was used to replace the missing skull section. A stainless-steel head holder was attached to the skull to head-fix the animal and to reduce motion-induced artifacts during imaging. Three weeks after virus injection, awake mice were habituated for 15 min in the treadmill-adapted imaging apparatus to minimize stress. The motor cortex was imaged at a depth of 100–200 µm below the pial surface using Prairie View 5.5.64.100 software with an Ultima Investigator two-photon microscope (Bruker) equipped with a ×16/0.80 NA water-immersion objective (Olympus) and an InSight X3 tunable laser (Spectra-Physics). An interlaced scan pattern model with a 920-nm tunable laser and a 1,040-nm fixed laser was used for sequential excitation. A 525/70-nm emission filter for NE2m and a 595/50-nm emission filter for rACh1h were used to collect the fluorescence signal. For the water licking paradigm, the animals were water-restricted for 2 days before imaging. During two-photon in vivo imaging, water was provided to the mouse 1 s after the initial lick and withheld for the subsequent 60 s, regardless of further licking. A custom Arduino code was used to record the capacitance changes due to licking and to control the water delivery. For flash stimulation, 30 pulses (0.2-s duration and 0.8-s interval) of white light were delivered. For auditory stimulation, a 30-s 7,000-Hz tone at 80 dB was delivered. For forced running, running speed was set at 15 cm s^{-1}. For image analysis, motion-related artifacts were corrected using EZcalcium[66]. FI was measured at the indicated regions of interest (ROIs) using ImageJ software. To measure $\Delta F/F_0$, F_0 was defined as the average baseline fluorescence signal measured for 10 s before the behavior onset. A Z-score was calculated by dividing $\Delta F/F_0$ by the standard deviation of the baseline. The peak response during a behavior was calculated as the average signal measured for 10 s (or 3 s for licking) around the maximum $\Delta F/F_0$ achieved after the behavior onset. For the area analysis in Extended Data Fig. 9i–k, a given brain area was deemed to be responsive if the average SNR in a 10-s window (for running) or a 3-s window (for licking) surrounding the peak exceeded 1.5× the value.

Immunohistochemistry

Mice were anesthetized with Avertin and intracardially perfused with PBS followed by 4% paraformaldehyde in PBS, and the brains were dissected and fixed at 4 °C overnight in 4% paraformaldehyde in PBS. The brains were then sectioned at 40-µm thickness using a VT1200 vibratome (Leica). The slices were placed in blocking solution containing 5% (v/v) normal goat serum, 0.1% Triton X-100 and 2 mM $MgCl_2$ in PBS for 30 min at room temperature. The slices were then incubated overnight at 4 °C in blocking solution containing 0.5% (v/v) normal goat serum, 0.1% Triton X-100 and 2 mM $MgCl_2$ in PBS with anti-GFP antibody (Abcam, catalog no. ab13970, chicken, dilution 1:500) and anti-RFP antibody (Rockland, catalog no. 600-401-379, rabbit, dilution 1:500). The following day, the slices were rinsed three times in blocking solution and then incubated for 2 h at room temperature with the following secondary antibodies: goat anti-chicken Alexa Fluor 488 (Abcam, catalog no. ab150169, dilution 1:1000) and goat anti-rabbit iFluor 555 (AAT Bioquest, catalog no. 16690, dilution 1:1000). After three washes in PBS, the slices were incubated in PBS containing DAPI (MedChemExpress, catalog no. HY-D0814, 5 mg ml^{-1}, dilution 1:1,000) for 15 min at room temperature, rinsed in PBS, mounted on slides and imaged using an Aperio VERSA slide scanner (Leica) equipped with a ×10 objective.

Statistics

Except where indicated otherwise, all summary data are presented as the mean ± s.e.m. Imaging data were analyzed using ImageJ version 1.53c or MATLAB R2020a and R2022a. Group data were plotted using OriginPro 2020b (OriginLab) or Prism 8.0.2 (GraphPad). The SNR was calculated by dividing the peak response by the standard deviation of the baseline fluorescence. Differences were analyzed using the two-tailed Student's t-test or one-way ANOVA; $^*P < 0.05$, $^{**}P < 0.01$, $^{***}P < 0.001$ and NS ($P \geq 0.05$).

Reporting summary

Further information on research design is available in the Nature Portfolio Reporting Summary linked to this article.

Data availability

The plasmids used to express the sensors in this study and the related sequences are available from Addgene (catalog nos. 234412–234419 and 251360; https://www.addgene.org/Yulong_Li/). The human G-protein-coupled receptor cDNA library was obtained from the hORFeome database 8.1 (http://horfdb.dfci.harvard.edu/index.php?page=home). Source data are provided with this paper.

Code availability

The custom-written MATLAB, Arduino and ImageJ programs are available under an MIT license from https://github.com/yulonglilab.

References

63. Gibson, D. G. et al. Enzymatic assembly of DNA molecules up to several hundred kilobases. *Nat. Methods* **6**, 343–345 (2009).
64. Pnevmatikakis, E. A. & Giovannucci, A. NoRMCorre: an online algorithm for piecewise rigid motion correction of calcium imaging data. *J. Neurosci. Methods* **291**, 83–94 (2017).
65. Ma, Y. et al. Wide-field optical mapping of neural activity and brain haemodynamics: considerations and novel approaches. *Philos. Trans. R. Soc. B* **371**, 20150360 (2016).
66. Cantu, D. A. et al. EZcalcium: open-source toolbox for analysis of calcium imaging data. *Front. Neural Circuits* **14**, 25 (2020).

Acknowledgements

This work was supported by grants from the National Key R&D Program of China (grant no. 2023YFE0207100), the National Natural Science Foundation of China (grant no. 32525003), Beijing Municipal

Science & Technology Commission (grant no. Z220009) and the NIH BRAIN Initiative (grant no. 1U01NS120824) to Y.L. and National Natural Science Foundation of China (grant nos. 82271210, 82471214) to C.W. Support was also provided by the Feng Foundation of Biomedical Research, the New Cornerstone Science Foundation through the New Cornerstone Investigator Program, the Peking-Tsinghua Center for Life Sciences, and the State Key Laboratory of Membrane Biology at Peking University School of Life Sciences (to Y.L.). We thank the optical imaging platform and small animal imaging platform of the National Center for Protein Sciences at Peking University in Beijing, China, for their support and assistance with the Operetta CLS high-content imaging system and the behavior facility; the Laboratory Animal Center of Peking University for advice and technical support; and X. Lei at PKU-CLS for assistance with the Opera Phenix high-content screening system. We thank the Cell Imaging Platform at Peking University Chengdu Academy for Advanced Interdisciplinary Biotechnologies for assistance with cellular imaging and J. Zhong for his technical support. We thank Z. Jiao from Xiaohong Xu lab at Center for Excellence in Brain Science and Intelligence Technology, Chinese Academy of Sciences, for recording and sharing the mating-related and pain-associated ultrasonic vocalization.

Author contributions

Y.L. supervised the study. S.X., J.F. and Y.L. designed the study. G.L., M.L., R.C. and L.G. performed the experiments related to the development, optimization and characterization of the sensors in cultured HEK293T cells and in neurons. S.X. and E.J. performed the surgery and two-photon imaging experiments related to the validation of the sensors in acute brain slices. X.M. and J.W. performed the in vivo fiber photometry recoding during optogenetic stimulation under the supervision of C.W. Y.Z. performed the in vivo fiber photometry recording in the NAc during foot shock and sucrose water delivery. X.M. performed the in vivo fiber photometry recording in the BLA during the Pavlovian conditioning task and in the dCA1 during sleep–wake cycles. S.X. performed the in vivo mesoscopic imaging and two-photon imaging of the cortex. S.L. performed immunohistochemistry experiments. All authors contributed to the interpretation and analysis of the data. S.X. and Y.L. wrote the manuscript with contributions from all authors.

Competing interests

The authors declare no competing interests.

Additional information

Extended data is available for this paper at https://doi.org/10.1038/s41593-026-02325-w.

Supplementary information The online version contains supplementary material available at https://doi.org/10.1038/s41593-026-02325-w.

Correspondence and requests for materials should be addressed to Changwei Wei or Yulong Li.

Peer review information *Nature Neuroscience* thanks Bernardo Sabatini, J. Simon Wiegert and the other, anonymous, reviewer(s) for their contribution to the peer review of this work.

https://doi.org/10.1038/s41593-026-02325-w

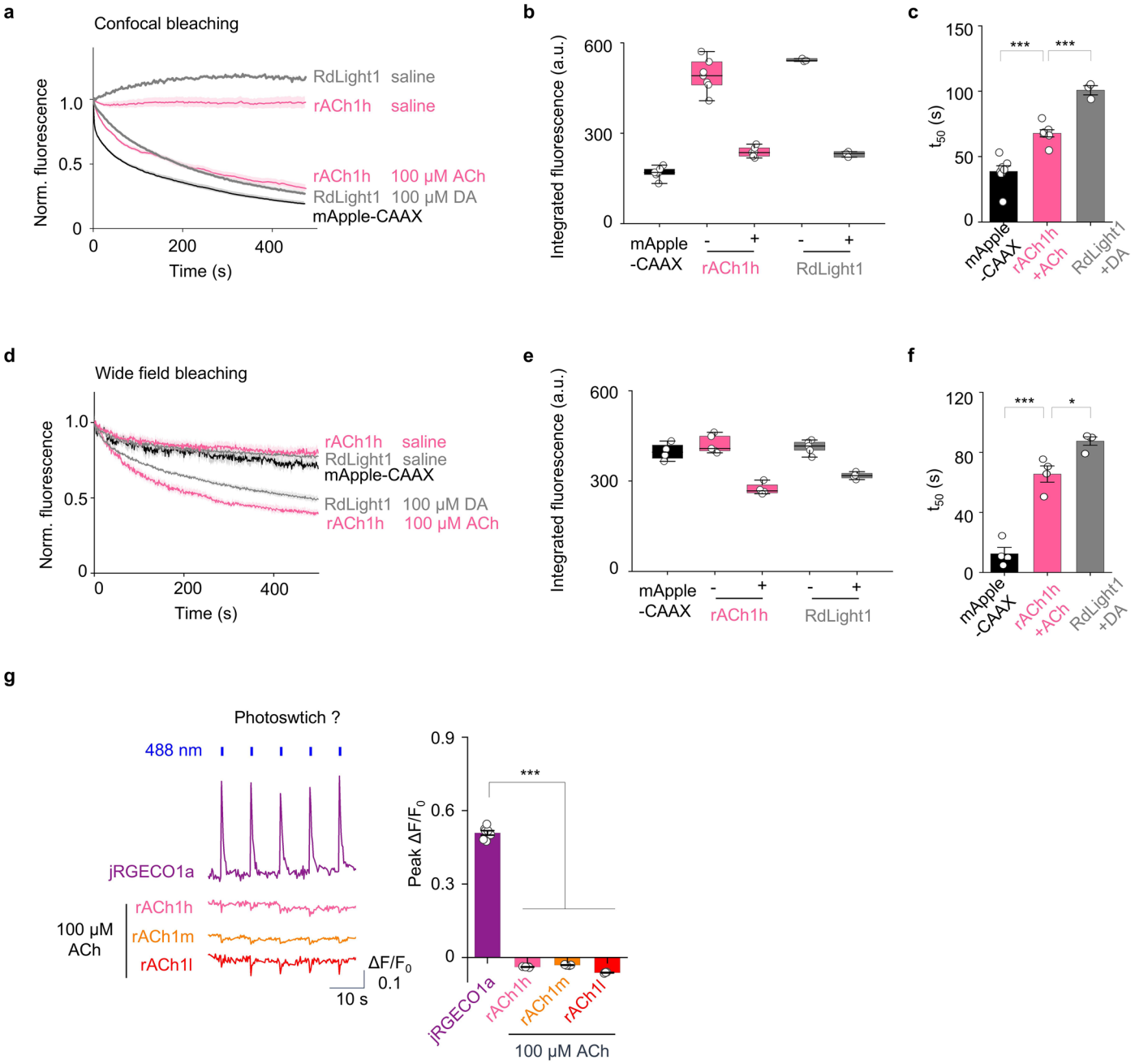

Extended Data Fig. 1 | Photostability and photoswitching of the rACh1h sensor. a, Normalized fluorescence intensity of mApple-CAAX, rACh1h (in the absence or presence of 100 μM ACh), or RdLight1[25] (in the absence or presence of 100 μM DA) during continuous confocal laser illumination, mean ± s.e.m. **b**, Integrated fluorescence of mApple-CAAX, or rACh1h and Rdlight1 shown in (**a**). Boxes show the first and third quartiles as well as the median. Whiskers show the maximum and minimum of each group. n = 7, 7 and 3 wells for mApple-CAAX, rACh1h and Rdlight1 respectively. **c**, Decay t_{50} of mApple-CAAX, or rACh1h and Rdlight1 during confocal laser illumination. mean ± s.e.m. n = 7, 7 and 3 wells for mApple-CAAX, rACh1h and Rdlight1 respectively. One-way ANOVA with post hoc Tukey's test was performed. Post hoc test: $P = 1.02\times10^{-4}$ for rACh1h versus mApple-CAAX, $P = 3.85\times10^{-4}$ for rACh1h versus Rdlight1. **d**, Normalized fluorescence intensity of mApple-CAAX, rACh1h (in the absence or presence of 100 μM ACh), or RdLight1 (in the absence or presence of 100 μM DA) during wide field LED illumination, mean ± s.e.m. **e**, Integrated fluorescence of mApple-CAAX, or rACh1h and Rdlight1 shown in (**d**) Boxes show the first and third quartiles as well as the median. Whiskers show the maximum and minimum of each group. n = 4 for mApple-CAAX, rACh1h and Rdlight1. **f**, Decay t_{50} of mApple-CAAX, or rACh1h and Rdlight1 during wide field laser bleaching, mean ± s.e.m. n = 4 for mApple-CAAX, rACh1h and Rdlight1. One-way ANOVA with post hoc Tukey's test was performed. Post hoc test: $P = 2.78\times10^{-5}$ for rACh1h versus mApple-CAAX, P = 0.014 for rACh1h versus Rdlight1. **g**, Representative traces (Left) and peak $\Delta F/F_0$ (Right) in response to blue light in cells expressing jRGECO1a, rACh1h, rACh1m and rACh1l after 100 μM ACh addition. mean ± s.e.m. n = 7, 4, 4 and 4 wells for jRGECO1a, rACh1h, rACh1m and rACh1l. One-way ANOVA with post hoc Tukey's test was performed, post hoc test: $P = 1\times10^{-676}$ for jRGECO1a versus rACh1h, rACh1m and rACh1l.

https://doi.org/10.1038/s41593-026-02325-w

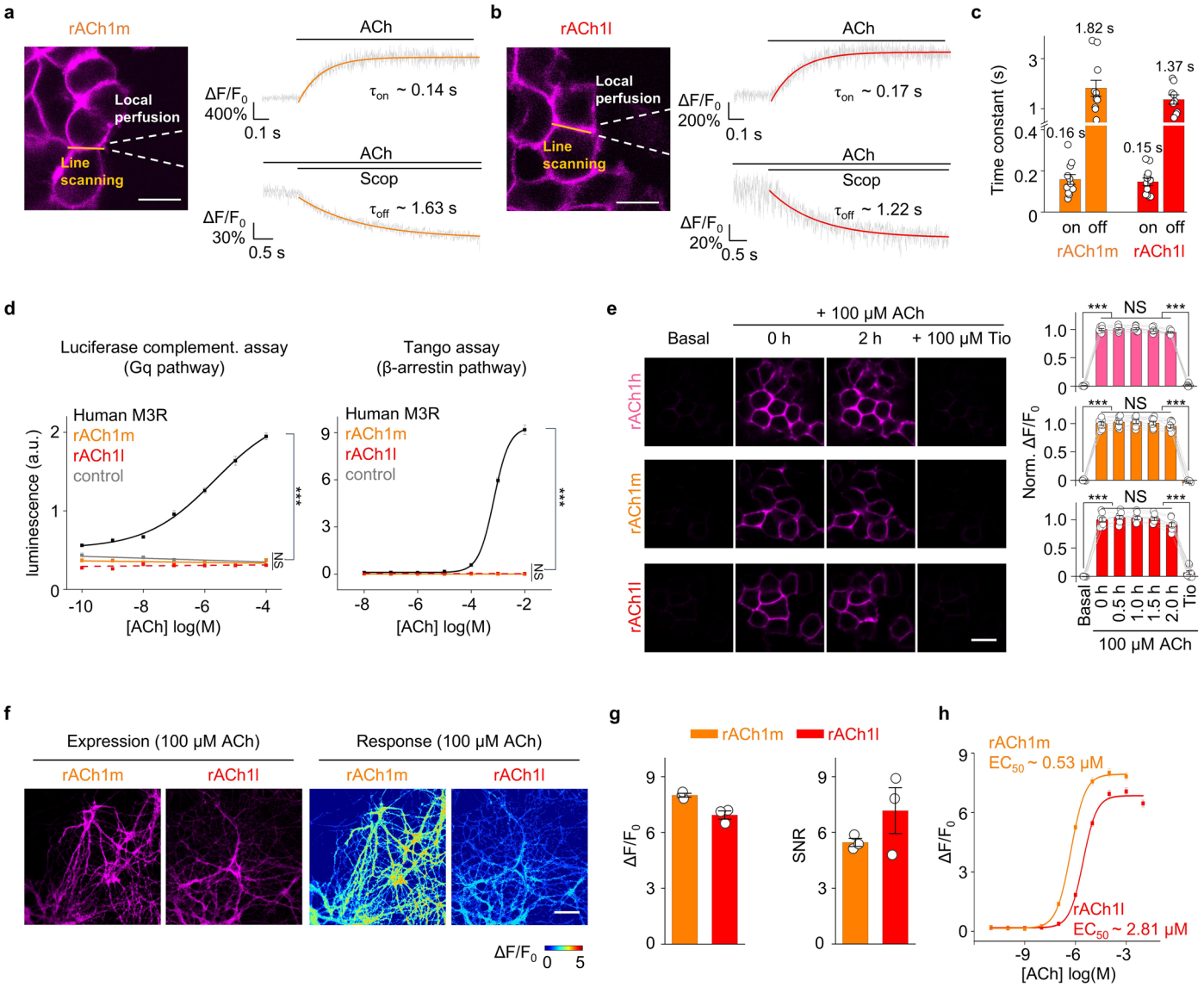

Extended Data Fig. 2 | Characterization of GRAB$_{ACh}$ sensors in cultured cells and neurons. a-b, Kinetics measurements of rACh1m and rACh1l. Schematic illustration showing the experimental setup of line-scanning and local puffing (Left), representative traces of sensor fluorescence increase in response to ACh (Right top) and decrease in response to Scop (Right bottom). **c**, Group summary of on and off kinetics for the sensors, mean ± s.e.m. n = 11 puff tests for on and off kinetics of rACh1m. n = 12 and 9 puff tests for on and off kinetics of rACh1l. **d**, Downstream coupling test. Human M3R; rACh1m; rACh1l; Control, without expression of WT M3R or sensors, mean ± s.e.m. n = 3 wells per group, One-way ANOVA with post hoc Tukey's test was performed. For the luciferase complementation assay, post hoc test: P = 1×10^{-406} for rACh1m and rACh1l versus Human M3R. For the tango assay, post hoc test: P = 1×10^{-389} for rACh1m and rACh1l versus Human M3R. **e**, Representative images and normalized $\Delta F/F_0$ of rACh1h, rACh1m and rACh1l in response to 100 μM ACh addition, followed by 100 μM Tio. n = 7,8 and 8 wells for rACh1h, rACh1m and rACh1l, mean ± s.e.m. One-way ANOVA with post hoc Tukey's test was performed. For rACh1h, rACh1m and rACh1l, P = 1×10^{-463}, P = 1×10^{-135} and P = 6.52×10^{-8} for baseline versus 0-2 h; P = 1×10^{-407}, P = 1×10^{-148} and P = 2.64×10^{-7} for 0-2 h versus Tio. **f**, Expression and response of rACh1m and rACh1l in cultured neurons with 100 μM ACh addition. Scale bar, 100 μm. **g**, Group summary of $\Delta F/F_0$ and SNR of rACh1m and rACh1l, mean ± s.e.m. n = 3 wells for each sensor. **h**, Dose-response curves for rACh1m and rACh1l, mean ± s.e.m. n = 3 wells for each sensor. EC_{50}, half-maximum effective concentration; NS, not significant.

https://doi.org/10.1038/s41593-026-02325-w

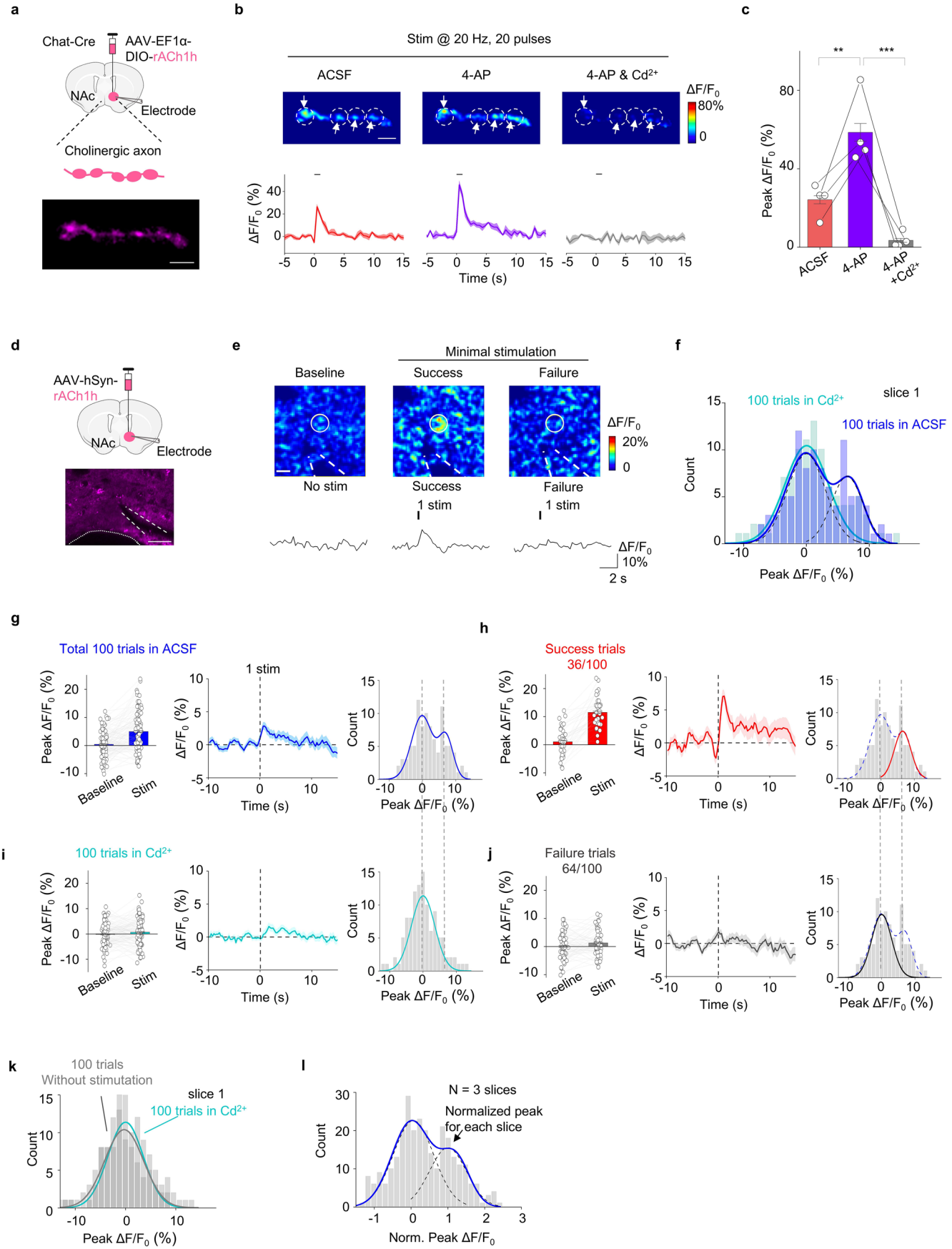

Extended Data Fig. 3 | See next page for caption.

https://doi.org/10.1038/s41593-026-02325-w

Extended Data Fig. 3 | rACh1h sensor reveals putative individual ACh release sites in NAc slices. a, Top: Schematic illustrating two-photon imaging of an acute brain slice from a ChAT-Cre mouse injected with AAV-EF1a-DIO-rACh1h for targeted expression of the rACh1h sensor on cholinergic axons. Bottom: Representative image showing rACh1h expression. Scale bar, 10 µm. Similar results were observed in 4 slices from 4 mice. **b**, Representative images and fluorescence traces of rACh1h response to electrical stimulation in ACSF, in the presence of the K^+ channel blocker 4-AP (100 µM), and after subsequent addition of the voltage-gated calcium channel blocker Cd^{2+} (200 µM), mean ± s.e.m. The dashed circles indicate the ROI used to calculate the response. The arrows indicate the individual release site. Scale bar, 10 µm. **c**, Group summary of the fluorescence change under the conditions shown in (**b**), mean ± s.e.m. n = 4 slices from 4 mice. One-way ANOVA with post hoc Tukey's test was performed, post hoc test: P = 0.006 for ACSF versus 4-AP and P = 2.5×10^{-14} for 4-AP versus 4-AP+Cd^{2+}. **d**, Schematic illustration and expression image depicting the two-photon imaging of minimal stimulation. Scale bar, 100 µm. **e**, Representative images and fluorescence traces of rACh1h response during minimal stimulation (left, baseline; middle, success trial; right, failure trial). White circles represent ROI for response analysis. Scale bar, 10 µm. **f**, Histogram showing the distribution of peak $\Delta F/F_0$ of rACh1h in 100 minimal-stimulation trials in ACSF and Cd^{2+}(200 µM). **g-j**, Detailed analysis of the 100 trials in ACSF or in Cd^{2+}. (**g**) the fluorescence responses (left), averaged traces (middle) and the distribution (right) of rACh1h in a total of 100 trials under minimal stimulation in ACSF, mean ± s.e.m. (**h**) Same analysis for the 31 trials classified as successes. These trials are highlighted in red in the distribution. (**i**) Same analysis for the 100 control trials in Cd^{2+}. These trials are highlighted in cyan in the distribution. (**j**) Same analysis for the 69 trials classified as failures. These trials are highlighted in black in the distribution. **k**, Distributions of peak $\Delta F/F_0$ from 100 without stimulation trials in ACSF and with stimulation in Cd^{2+}. **l**, Pooled distribution of normalized peak $\Delta F/F_0$ responses from all minimal stimulation experiments (n = 300 trials from 3 slices, 3 mice). Illustrations in **a** and **d** created in BioRender; Li, Y. https://biorender.com/xngrhc6 (2026).

https://doi.org/10.1038/s41593-026-02325-w

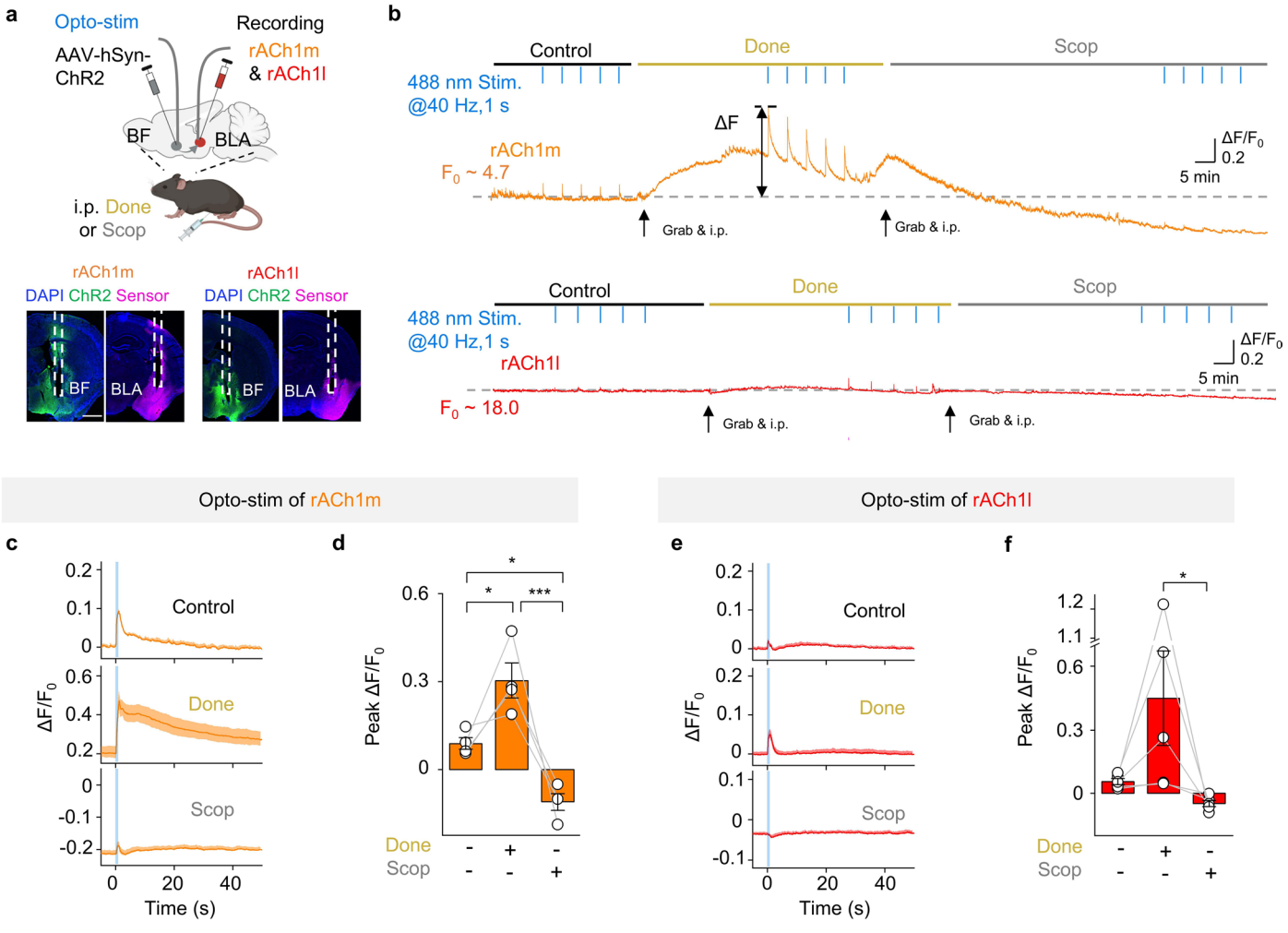

Extended Data Fig. 4 | Performance of red GRAB$_{ACh}$ sensors in vivo. a, Schematic illustration and expression images depicting the fiber-photometry recording involving red ACh sensors for panel **b-f**. Scale bar, 1 mm. **b**, Representative traces of rACh1m and rACh1l in response to optical stimulation in the BF before (Control, left), after an i.p. injection of the AChE inhibitor donepezil (Done, 3 mg/kg, middle), and after an i.p. injection of the M3R antagonist scopolamine (Scop, 10 mg/kg, right). **c**, Representative trace of fluorescence change of rACh1m to optogenetic stimulation, mean ± s.e.m. **d**, Group summary of fluorescence change in rACh1m to optogenetic stimulation, mean ± s.e.m. n = 4 mice for rACh1m. One-way ANOVA with post hoc Tukey's test was performed, post hoc test: P = 0.011 for control versus Done; P = 0.016 for control versus Scop; P = 1.3×10^{-6} for Scop versus Done. **e**, Representative trace of fluorescence change of rACh1l to optogenetic stimulation, mean ± s.e.m. **f**, Group summary of fluorescence change in rACh1l to optogenetic stimulation, mean ± s.e.m. n = 5 mice for rACh1l. One-way ANOVA with post hoc Tukey's test was performed, post hoc test: P = 0.046 for Scop versus Done. **g**, Representative absolute fluorescence intensity traces of red ACh sensors in response to optical stimulation in the BF. **h**, Group summary of baseline fluorescence between red ACh sensors, mean ± s.e.m. n = 3 mice for sham, n = 3 mice for rACh1h, n = 4 mice for rACh1m, n = 5 mice for rACh1l and n = 3 mice for rAChmut. Two-tailed Student's t tests: P = 0.002, 0.011, 0.013 and 0.025 for rACh1h, rACh1m, rACh1l and rAChmut versus sham group. Illustration in **a** created in BioRender; Li, Y. https://biorender.com/xngrhc6 (2026).

https://doi.org/10.1038/s41593-026-02325-w

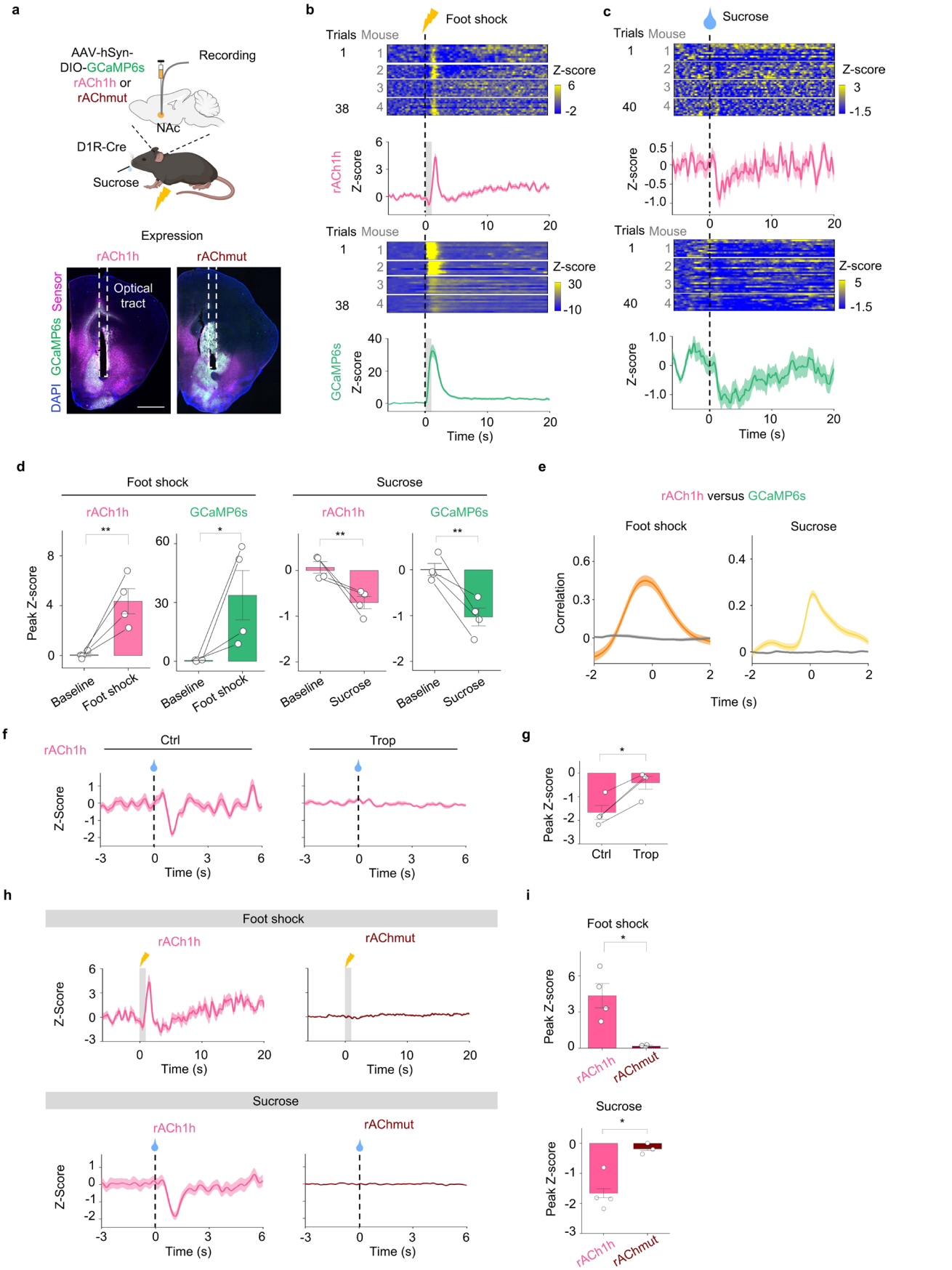

Extended Data Fig. 5 | See next page for caption.

https://doi.org/10.1038/s41593-026-02325-w

Extended Data Fig. 5 | Multiplex measurements of ACh with calcium. a, Top, Schematic illustration depicting the multiplex recording of rACh1h or rAChmut with GCaMP6s in foot shock and reward task. Bottom, expression images of rACh1h or rAChmut with GCaMP6s in NAc. Scale bar, 1 mm. **b-c**, Heatmap and representative traces of rACh1h and GCaMP6s in foot shock and reward task (38 trials in foot shock and 40 trials in reward task from 4 mice), mean ± s.e.m. **d**, Group summary of fluorescence change of rACh1h and GCaMP6s signals, mean ± s.e.m. n = 4 mice for foot shock and reward task. Two-tailed Student's t tests were performed. P = 0.006 of rACh1h and P = 0.039 of GCaMP6s before and after foot shock; P = 0.006 of rACh1h and P = 0.005 of GCaMP6s before and after reward. **e**, The average cross-correlation between rACh1h and GCaMP6s signals during foot shock and reward task, mean ± s.e.m. n = 4 mice. **f**, The representative traces of rACh1h in foot shock before and after muscarinic receptor antagonist tropicamide (Trop, 10 mg/kg) administration, mean ± s.e.m. **g**, Group summary of rACh1h signals in (**f**). mean ± s.e.m. n = 4 mice. Two-tailed Student's t tests were performed. P = 0.013 before and after blocker injection. **h**, The representative traces of rACh1h and rAChmut during foot shock and reward task, mean ± s.e.m. **i**, Group summary of rACh1h and rAChmut signals in (**h**), mean ± s.e.m. n = 4 mice for rACh1h and n = 3 mice for rAChmut. Two-tailed Student's t tests were performed. During foot shock, P = 0.017 between rACh1h and rAChmut. During reward task, P = 0.009 between rACh1h and rAChmut. Illustration in **a** created in BioRender; Li, Y. https://biorender.com/xngrhc6 (2026).

https://doi.org/10.1038/s41593-026-02325-w

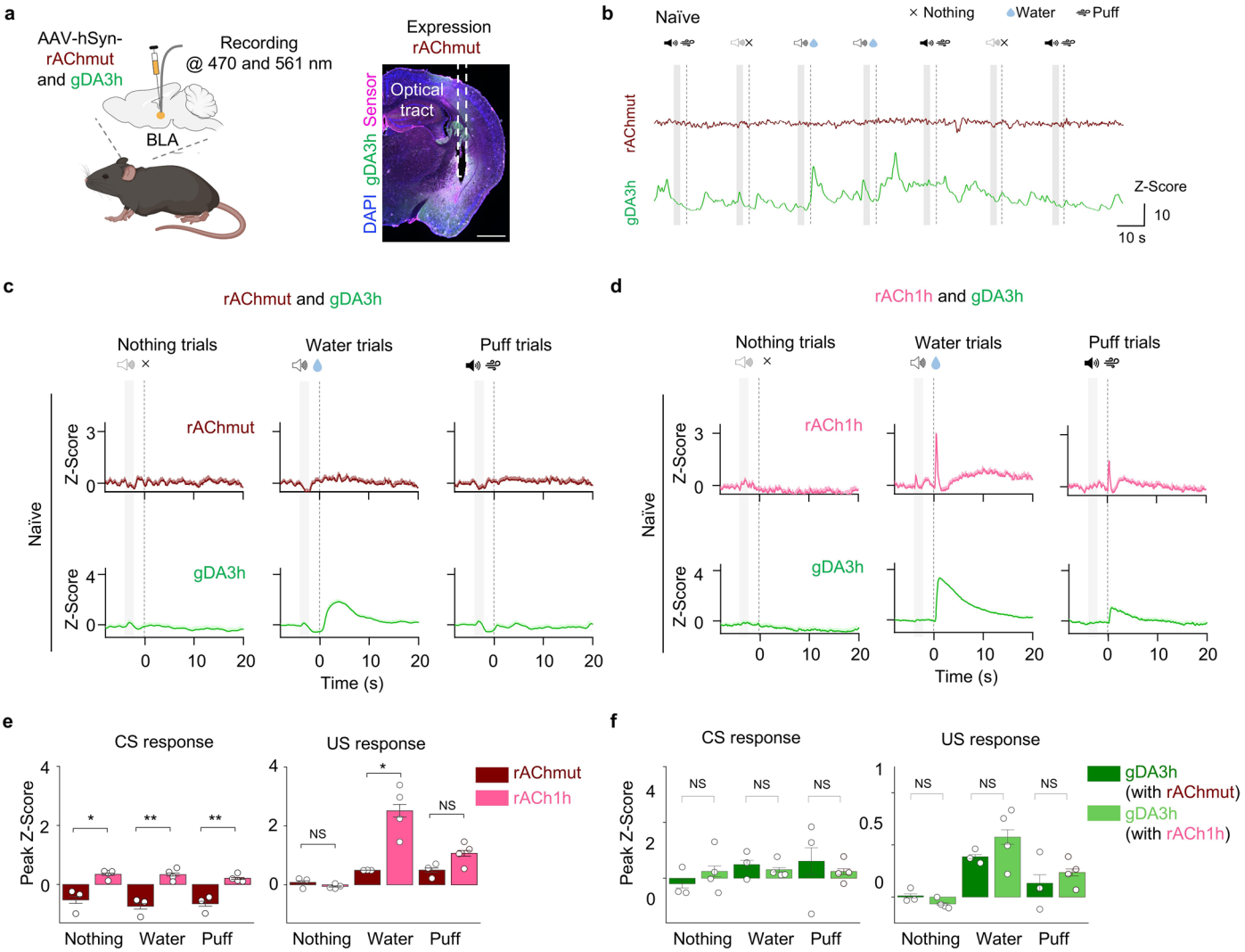

Extended Data Fig. 6 | Representative rAChmut and gDA3h signals during Pavlovian. a, Left, schematic illustration depicting the recording involving rAChmut and gDA3h during Pavlovian conditioning tasks. Right, expression image of rAChmut and gDA3h. Scale bar, 1 mm. **b**, Representative traces of rAChmut (dark red) and gDA3h (green) simultaneously measured in BLA during seven consecutive trials. **c**, Representative averaged traces of rAChmut and gDA3h fluorescence from a mouse in naïve state. **d**, Representative averaged traces of rACh1h and gDA3h fluorescence from a mouse in naïve state (from Fig. 3c). **e**, Group summary of rACh1h and rAChmut signals to CS (left) and US (right), mean ± s.e.m. n = 4 mice for rACh1h and n = 3 mice for rAChmut. Two-tailed Student's t tests were performed. For US, P = 0.010 in water trial. For CS, P = 0.010, 0.003 and 0.003 in nothing, water and puff trials respectively. **f**, Group summary of gDA3h with rACh1h or rAChmut signals to CS (left) and US (right), mean ± s.e.m. n = 4 mice for the group with rACh1h and n = 3 mice for the group with rAChmut. Two-tailed Student's t tests were performed. NS, not significant. Illustration in **a** created in BioRender; Li, Y. https://biorender.com/xngrhc6 (2026).

https://doi.org/10.1038/s41593-026-02325-w

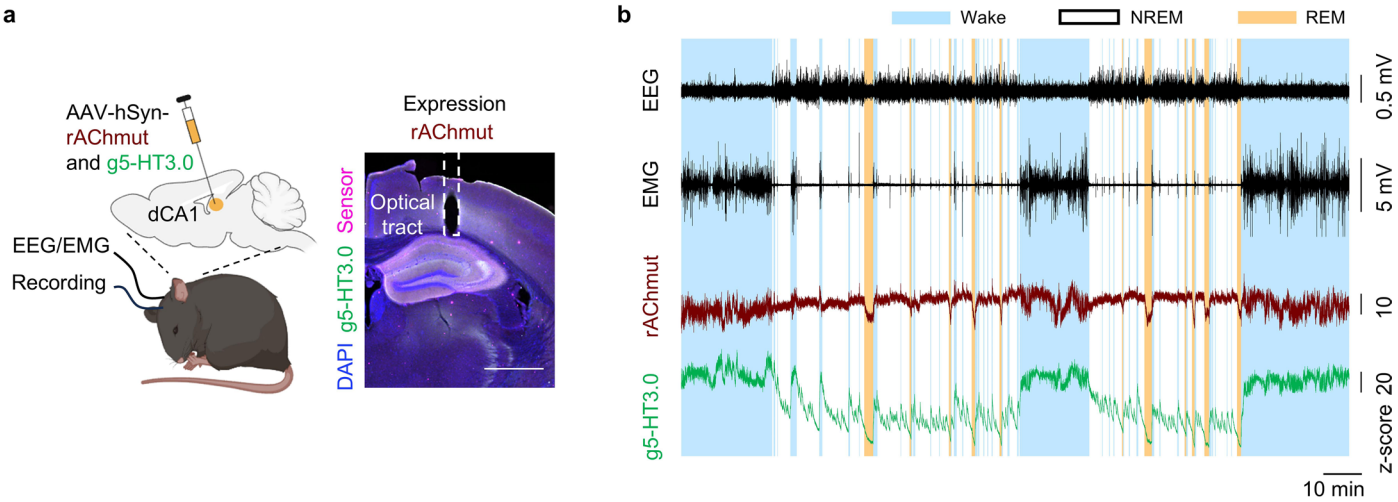

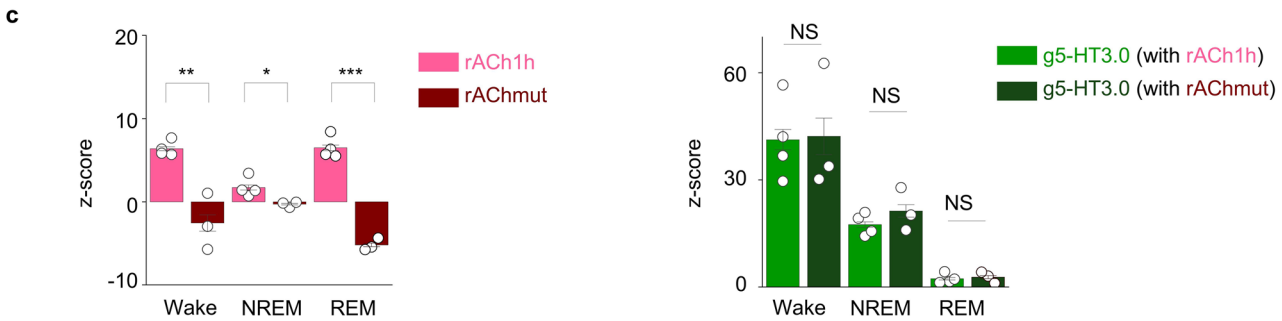

Extended Data Fig. 7 | Representative rAChmut and g5-HT3.0 signals during the sleep-wake cycle in freely moving mice. a, Schematic illustration and expression image depicting the dual-color recording involving rAChmut and g5-HT3.0 during sleep-wake cycles for panel **b-c**. Scale bar, 1 mm. **b**, Representative traces of EEG, EMG, rAChmut (dark red) and g5-HT3.0 (green) during sleep-wake cycles in freely behaving mice. Blue shading, wake state; orange shading, REM sleep. **c**, Group summary of rAChmut and g5-HT3.0 fluorescence in dCA1 compared to rACh1h during the wake state, NREM sleep, and REM sleep. The data of rACh1h and g5-HT3.0 (with rACh1h) is replotted from Fig.3c, mean ± s.e.m. n = 4 mice for rACh1h and n = 3 mice for rAChmut. Two-tailed Student's t tests were performed. For rACh1h versus rAChmut, P = 0.003 during Wake, P = 0.037 between during NREM, P = 4.0×10^{-5} between during REM. NS, not significant. Illustration in **a** created in BioRender; Li, Y. https://biorender.com/xngrhc6 (2026).

https://doi.org/10.1038/s41593-026-02325-w

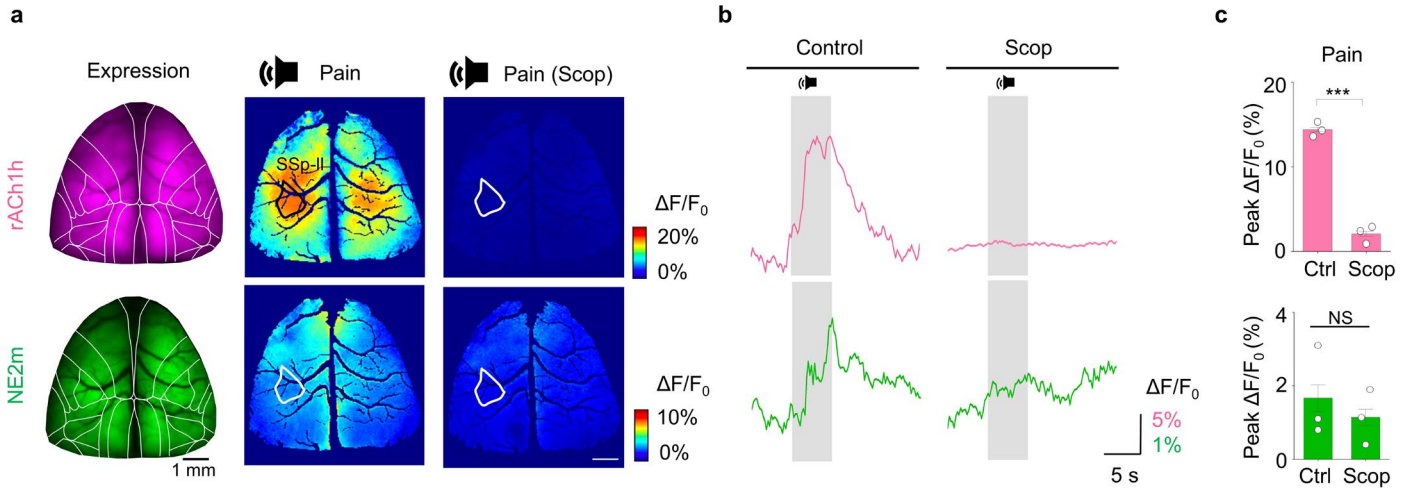

Extended Data Fig. 8 | rACh1h and NE2m signals before and after Scop injection during pain auditory stimulation. a, Expression and pseudocolor images of rACh1h and NE2m during pain vocalization. The Allen Common Coordinate Framework v3 (CCFv3) atlas was used for anatomical alignment. The polygon outlines in the pseudocolor images enclose the ROI for response. Scale bar, 1 mm. **b**, Representative traces of rACh1h and NE2m response during pain vocalization before and after scopolamine (Scop, 10 mg/kg) administration. **c**, Quantifications of peak $\Delta F/F_0$ in SSp-ll for rACh1h and NE2m during pain vocalization, mean ± s.e.m. n = 3 mice. Two-tailed Student's t tests were performed. $P = 9.28 \times 10^{-5}$ of rACh1h between Ctrl and Scop. NS, not significant.

https://doi.org/10.1038/s41593-026-02325-w

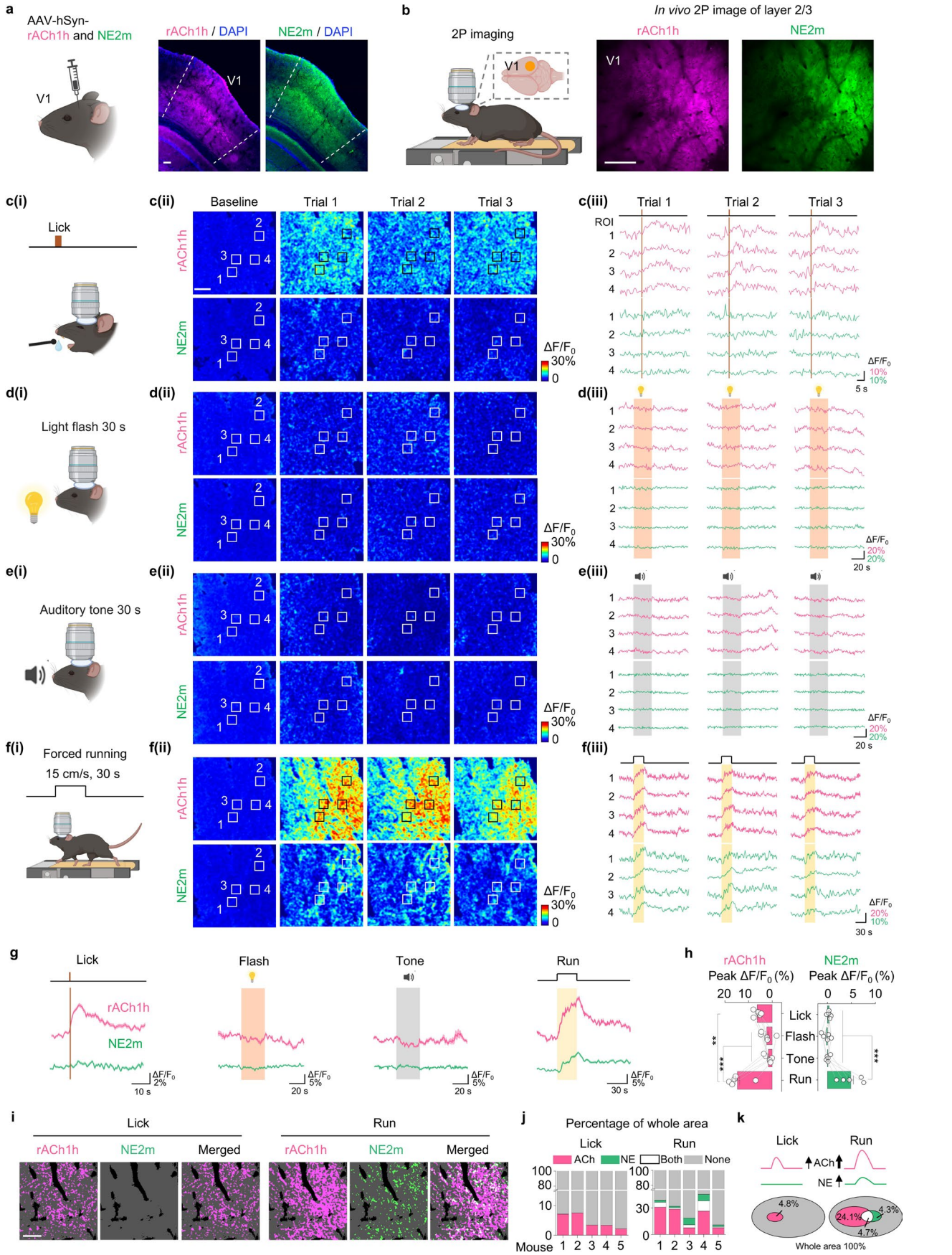

Extended Data Fig. 9 | See next page for caption.

https://doi.org/10.1038/s41593-026-02325-w

Extended Data Fig. 9 | Two-photon imaging of cortical ACh and NE dynamics. **a**, Schematic illustration (Left) depicting the viral injection. Representative image (Right) showing the expression of rACh1h and NE2m in coronal brain slice. Scale bar, 100 µm. Similar results were observed in 5 mice. **b**, Schematic illustration (Left) depicting the head-fixed two-photon imaging at V1 cortex. Example in vivo two-photon images of layer 2/3 in the V1 cortex (Right) showing rACh1h and NE2m fluorescence. Scale bar, 100 µm. Similar results were observed in 5 mice. **c**, Schematic cartoon illustrating water licking task (**c(i)**), representative response images (**c(ii)**) and typical traces (**c(iii)**) during three trials for rACh1h (Top) and NE2m (Bottom). Scale bar, 100 µm. **d-f**, Similar to **c**, the illustration, response images and traces in light flash (**d**), auditory tone (**e**) and forced running (**f**). Two-photon imaging was performed in the same region across behaviors. **g**, Averaged traces of rACh1h and NE2m in different behaviors, mean ± s.e.m. **h**, Quantifications of peak $\Delta F/F_0$ for rACh1h and NE2m during different behaviors, mean ± s.e.m. n = 5 mice. One-way ANOVA with post hoc Tukey's test was performed. For rACh1h, post hoc test: $P = 1.7\times10^{-5}$ and 8.7×10^{-6} for Run versus Tone and Flash. For NE2m, post hoc test: $P = 2.4\times10^{-4}$, 6.8×10^{-5} and 1.4×10^{-4} for Run versus Lick, Flash and Tone. **i**, Representative images showing the spatial pattern for rACh1h and NE2m to lick and run. **j**, Percentage summary of the response area from 5 mice for rACh1h and NE2m to lick and run. **k**, Summary and Venn diagram for rACh1h and NE2m responding to lick and run. Illustrations in **a**–**f** created in BioRender; Li, Y. https://biorender.com/xngrhc6 (2026).

https://doi.org/10.1038/s41593-026-02325-w

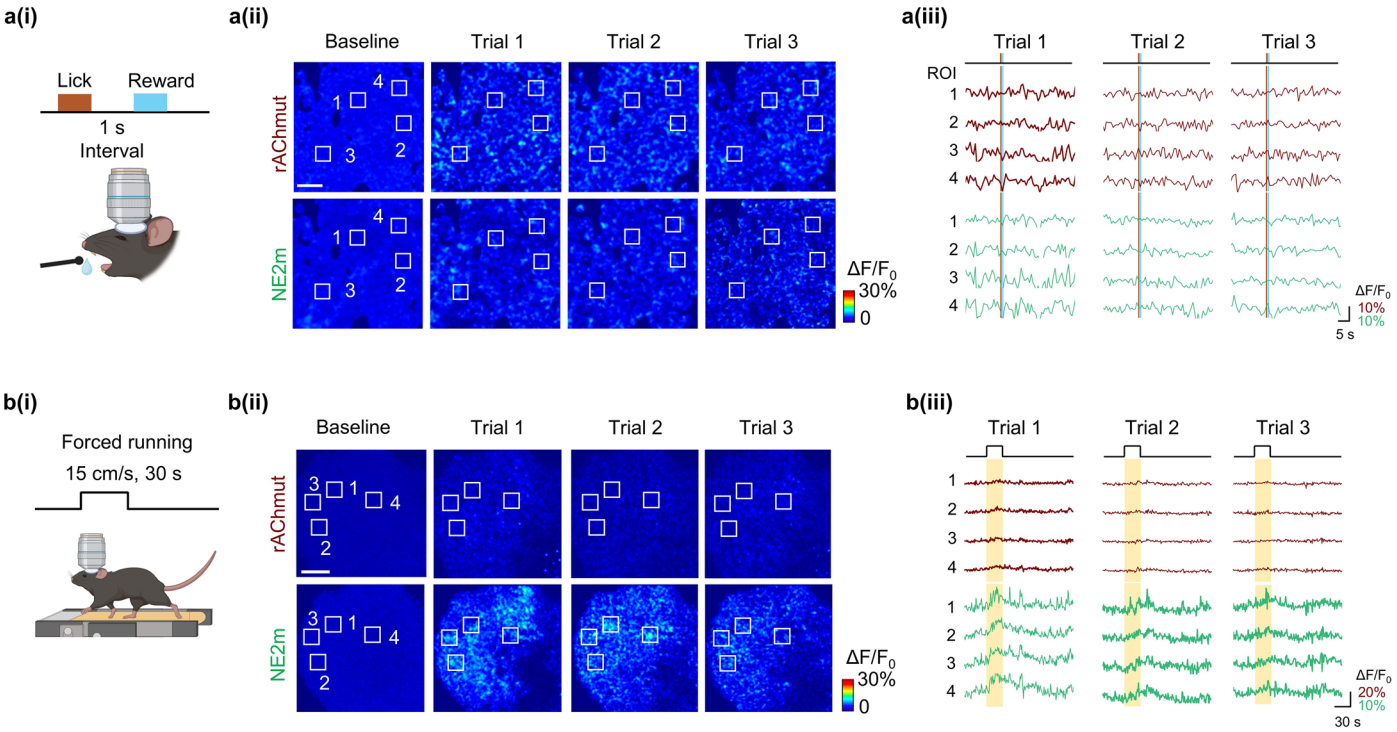

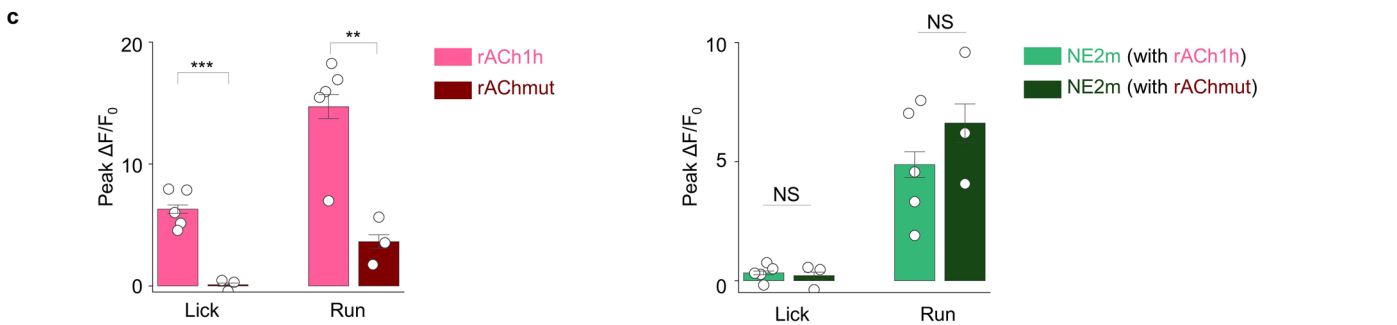

Extended Data Fig. 10 | Representative rAChmut and NE signals in the cortex. **a**, Schematic cartoon illustrating water licking task (**a(i)**) (Created in BioRender; Li, Y. https://BioRender.com/xngrhc6 (2026)), representative response images (**a(ii)**) and typical traces (**a(iii)**) during three trials for rAChmut (Top) and NE2m (Bottom). Scale bar, 100 µm. **b**, Schematic cartoon illustrating forced running (**b(i)**) (Created in BioRender; Li, Y. https://BioRender.com/xngrhc6 (2026)), representative response images (**b(ii)**) and typical traces (**b(iii)**) during three trials for rAChmut (Top) and NE2m (Bottom). Scale bar, 100 µm. **c**, Group summary of rAChmut and NE2m peak response compared to rACh1h during the licking and running. The data of rACh1h and NE2m (with rACh1h) is replotted from Fig.4h, mean ± s.e.m. n = 5 mice for rACh1h and n = 3 mice for rAChmut. Two-tailed Student's t tests were performed. For rACh1h versus rAChmut, $P = 6.0\times10^{-4}$ in licking, P = 0.007 in running. NS, not significant. Illustrations in **a** and **b** created in BioRender; Li, Y. https://biorender.com/xngrhc6 (2026).

nature portfolio

Corresponding author(s): Yulong Li

Last updated by author(s): Mar 19, 2026

Reporting Summary

Nature Portfolio wishes to improve the reproducibility of the work that we publish. This form provides structure for consistency and transparency in reporting. For further information on Nature Portfolio policies, see our Editorial Policies and the Editorial Policy Checklist.

Statistics

For all statistical analyses, confirm that the following items are present in the figure legend, table legend, main text, or Methods section.

n/a	Confirmed
☐	☒ The exact sample size (*n*) for each experimental group/condition, given as a discrete number and unit of measurement
☐	☒ A statement on whether measurements were taken from distinct samples or whether the same sample was measured repeatedly
☐	☒ The statistical test(s) used AND whether they are one- or two-sided *Only common tests should be described solely by name; describe more complex techniques in the Methods section.*
☒	☐ A description of all covariates tested
☐	☒ A description of any assumptions or corrections, such as tests of normality and adjustment for multiple comparisons
☐	☒ A full description of the statistical parameters including central tendency (e.g. means) or other basic estimates (e.g. regression coefficient) AND variation (e.g. standard deviation) or associated estimates of uncertainty (e.g. confidence intervals)
☐	☒ For null hypothesis testing, the test statistic (e.g. *F*, *t*, *r*) with confidence intervals, effect sizes, degrees of freedom and *P* value noted *Give P values as exact values whenever suitable.*
☒	☐ For Bayesian analysis, information on the choice of priors and Markov chain Monte Carlo settings
☒	☐ For hierarchical and complex designs, identification of the appropriate level for tests and full reporting of outcomes
☒	☐ Estimates of effect sizes (e.g. Cohen's *d*, Pearson's *r*), indicating how they were calculated

Our web collection on statistics for biologists contains articles on many of the points above.

Software and code

Policy information about availability of computer code

Data collection	1.The NIS-Element 4.51.00 software of Ti-E A1 confocal microscope (Nikon) 2. The Prairie View 5.5 software of Ultima Investigator 2-photon microscope (Bruker) 3. The Harmony 4.9 software of Opera Phenix high-content screening system (Perkin Elmer) 4. The Multi channel Fiber Photometry software of the fiber-photometry system (Thinkerbiotech, china) 5. The inper signal V2.0.0 software of the fiber-photometry system (Inper, China)
Data analysis	1.ImageJ version1.53c 2.Matlab R2020a and R2022a 3.OriginPro 2020b 4.GraphPad Prism 8.0.2 5.Adobe Illustrator CC 6.EZcalcium motion correction algorithm

For manuscripts utilizing custom algorithms or software that are central to the research but not yet described in published literature, software must be made available to editors and reviewers. We strongly encourage code deposition in a community repository (e.g. GitHub). See the Nature Portfolio guidelines for submitting code & software for further information.

Data

Policy information about availability of data

All manuscripts must include a data availability statement. This statement should provide the following information, where applicable:

- Accession codes, unique identifiers, or web links for publicly available datasets
- A description of any restrictions on data availability
- For clinical datasets or third party data, please ensure that the statement adheres to our policy

human (hORFeome database 8.1); The plasmids and sequences used to express the sensors in this study are available from Addgene (catalog nos. 234412 to234419 and 251360; Source data are provided with the paper.

Research involving human participants, their data, or biological material

Policy information about studies with human participants or human data. See also policy information about sex, gender (identity/presentation), and sexual orientation and race, ethnicity and racism.

Reporting on sex and gender	N/A
Reporting on race, ethnicity, or other socially relevant groupings	N/A
Population characteristics	N/A
Recruitment	N/A
Ethics oversight	N/A

Note that full information on the approval of the study protocol must also be provided in the manuscript.

Field-specific reporting

Please select the one below that is the best fit for your research. If you are not sure, read the appropriate sections before making your selection.

☒ Life sciences ☐ Behavioural & social sciences ☐ Ecological, evolutionary & environmental sciences

For a reference copy of the document with all sections, see nature.com/documents/nr-reporting-summary-flat.pdf

Life sciences study design

All studies must disclose on these points even when the disclosure is negative.

Sample size	No statistical methods were used to predetermine sample size. We used similar sample sizes to the literatures in the field. [1] Jing, Miao, et al. "A genetically encoded fluorescent acetylcholine indicator for in vitro and in vivo studies." Nature biotechnology 36.8 (2018): 726-737. [2] Sun, F., Zeng, J., Jing, M., Zhou, J., Feng, J., Owen, S. F., ... & Li, Y. (2018). A genetically encoded fluorescent sensor enables rapid and specific detection of dopamine in flies, fish, and mice. Cell, 174(2), 481-496. [3] Feng, Jiesi, et al. "A genetically encoded fluorescent sensor for rapid and specific in vivo detection of norepinephrine." Neuron 102.4 (2019): 745-761. [4]Zhuo, Y. et al. Improved green and red GRAB sensors for monitoring dopaminergic activity in vivo. Nat Methods 1–12 (2023) doi:10.1038/s41592-023-02100-w.
Data exclusions	No data were excluded for the analysis.
Replication	Each experiment in this manuscript is reliably reproduced. The replication number of each experiment is indicated in the legend of corresponding figures.
Randomization	Animals or cells were randomly assigned into control or experimental groups.
Blinding	The investigators were not blind to group allocation during data collection and analysis. The experimental conditions were obvious to the researchers and the analysis were performed objectively and not subjective to human bias.

Reporting for specific materials, systems and methods

We require information from authors about some types of materials, experimental systems and methods used in many studies. Here, indicate whether each material, system or method listed is relevant to your study. If you are not sure if a list item applies to your research, read the appropriate section before selecting a response.

Materials & experimental systems

n/a	Involved in the study
☐	☒ Antibodies
☐	☒ Eukaryotic cell lines
☒	☐ Palaeontology and archaeology
☐	☒ Animals and other organisms
☒	☐ Clinical data
☒	☐ Dual use research of concern
☒	☐ Plants

Methods

n/a	Involved in the study
☒	☐ ChIP-seq
☒	☐ Flow cytometry
☒	☐ MRI-based neuroimaging

Antibodies

Antibodies used

Primary antibodies:
1. chicken anti-GFP(1:500, Abcam, Cat # ab13970)
2. rabbit anti-RFP (1:500, Rockland, Cat # 600-401-379)
Secondary antibodies:
1. Alexa Fluor® 488 goat anti-chicken lgY (H+L)(1:1000, Abcam, Cat # ab150169)
2. iFluor® 555 goat anti-rabbit lgG (H+L)(1:1000, AAT Bioquest, Cat # 16690)

Validation

All antibodies were validated by the manufacturer and published research articles.
Chicken anti-GFP antibody (Abcam) used in immunofluorescence has been verified in Al-Moved H, et al., EMB0 Mol Med, 2019 and Handara G,et al, eLife,2015.
Rabbit anti-RFP antibody (Rockland) used in immunofluorescence has been verified in Rivera JF et al.,Nat Methods, 2025 and Coronado PER et al., Cell, 2025

Eukaryotic cell lines

Policy information about cell lines and Sex and Gender in Research

Cell line source(s)

HEK293T cells used in this paper were purchased from ATCC. The HEK293 cell line stably expressing a tTA-dependent luciferase reporter and the β-arrestin2-TEV fusion gene used in the TANGO assay was a generous gift from Bryan L. Roth.

Authentication

We have verified the cell line based on their morphology under microscope and an analysis of their growth curve.

Mycoplasma contamination

No mycoplasma contamination.

Commonly misidentified lines
(See ICLAC register)

No commonly misidentified cell lines were used.

Animals and other research organisms

Policy information about studies involving animals; ARRIVE guidelines recommended for reporting animal research, and Sex and Gender in Research

Laboratory animals

For cultured neurons, both male and female postnatal day 0 (P0) Sprague-Dawley rats were used.
For fiber photometry recording experiments, either adult wild-type C57BL/6J (Beiing vital River laboratory) or D1R-Cre (The JacksonLaboratory) mice were used.
For acute mouse brain slice, mesoscopic imaging and two-photon imaging experiments, adult wild-type C57BL/6J mice (6-8 weeks of age) were used.
All mice were group-housed or pair-housed in a temperature 18-23 'c), humidity (40-60% and light/dark cycle 112-h/12-hcontrolled room,with food and water available ad libitum.

Wild animals

No wild animals were used in the study.

Reporting on sex

Both male and female mice were used in the study, as indicated in the manuscript.

Field-collected samples

No field-collected samples were used in the study.

Ethics oversight

All procedures for animal surgery and maintenance were performed using protocols that were approved by the Animal Care & Use Committees at Peking University.

Note that full information on the approval of the study protocol must also be provided in the manuscript.

Plants

Seed stocks	N/A
Novel plant genotypes	N/A
Authentication	N/A